An Integrated RANS-PSE-Wave Packet Tool for the Prediction of Subsonic and Supersonic Jet Noise

Foluso Ladeinde[1] and Ken Alabi[2]
TTC Technologies, Inc., Stony Brook, NY, 11790

Tim Colonius [3] and Kristjan Gudmundsson[4]
California Institute of Technology, Pasadena, CA

Robert H. Schlinker[5] and Ramons A. Reba[6]
United Technologies Research Center, East Hartford, CT 06108

Few engineering tools are suitable for predicting supersonic jet noise, and the development of engine exhaust noise reduction technology for tactical aircraft continues to rely heavily on laboratory scale parametric testing. Aside from intuition and experience with the generally subtle issues involved in low-noise design, there is currently no way to rapidly and cheaply assess whether proposed designs will be effective, and no way to determine whether such designs are optimal. Arguably, this gap in jet noise modeling capability is an impediment toward achieving significant noise reduction for tactical aircraft. The objective of the on-going research program presented in this paper is to develop and demonstrate innovative, highly-efficient computational methodologies for simultaneous nozzle acoustic and aerodynamic design applicable to subsonic and supersonic jet exhaust noise reduction in tactical aircraft. The approach comprises of three major elements: (1) Reynolds-averaged Navier-Stokes (RANS)-CFD for computing the jet turbulent mean flow, (2) pressure wave packet-based methods for predicting near-field sound generation from the largest scales, based on the Linear Parabolized Stability Equations (LPSE) and the aforementioned RANS solutions, and (3) a method based on the solution of the linear wave equation for determining the acoustic radiation field from the LPSE solution. While these three procedures have received significant attention in the literature, their integration into a single tool for far-field noise prediction has not. To assess the accuracy and robustness of the simulation tool, experimental data has been acquired with near field array directed at detecting changes in the organized turbulence scale structure to link cause (nozzle geometry) and effect (near field and far field noise changes). Both ideally- and non-ideally expanded conditions are being investigated. Forward flight effects have also been measured using an open jet acoustic wind tunnel (at United Technologies Research Center) to evaluate the noise dependence on different operating conditions. The development and preliminary validation of the integrated tool is presented in this paper, with a focus on individual components and their translation into a common format for integration.

Nomenclature

3D	= three-dimensional	*LES*	= large-eddy simulation
F	= computational flux	*m*	= mode number
G	= Green's function	*M*	= Mach number
J	= Jacobian of transformation	*P, p*	= pressure, power spectral density *(P)*
k	= kinetic energy of turbulence	*Q*	= solution vector
R	= correlation function	*RANS*	= Reynolds-averaged Navier-Stokes

---

[1] Director of Research, AIAA Life Member and Associate Fellow
[2] Research Engineer, AIAA Member
[3] Professor, AIAA Associate Fellow
[4] AIAA Member
[5] Project Leader, Components, AIAA Associate Fellow
[6] Senior AIAA Member

SA	= Spalart-Allmaras	*St*	= Strouhal number
t	= time	*Λ*	= eigenvalue
T	= temperature	*γ*	= ratio of specific heats
TVD	= total-variation diminishing		
U	= velocity		
Ū	= mean velocity		
u	= velocity	Subscripts	
VLES	= very large-eddy simulation		
w	= WENO weight	*i*	= nodal point in finite difference
WENO	= weighted essentially non-oscillatory	*L*	= left
φ	= generic variable	*R*	= right
x	= axial direction	*M*	= mode
α	= spectral radius	*jet*	= related to jet exit conditions
δ	= Kronica delta	∞	= free stream
ε	= kinetic energy dissipation rate	'	= fluctuating
θ	= azimuthal angle		

I. Introduction

There are few engineering tools suitable to predict supersonic jet noise, and the development of engine exhaust noise reduction technology for tactical aircraft continues to rely heavily on laboratory-scale testing. In this absence of modeling and analysis capability, concept identification relies largely on engineering intuition, ad hoc reasoning, and exhaustive parametric testing. Aside from intuition and experience with the generally subtle issues involved in low-noise design, there is currently no way to rapidly and cheaply assess whether proposed designs will be effective, and no way to determine whether such designs are optimal. Arguably, this gap in jet noise modeling capability is an impediment toward achieving significant noise reduction for tactical aircraft.

A further impediment to exhaust noise technology development is the absence of integrated tools for simultaneous assessment of aero-acoustic and aerodynamic performance. As a result, non-acoustic design objectives tend to be considered later in the noise concept design process, with laboratory-scale tests proceeding without assessing the impact on nozzle thrust, aircraft stability, IR signature, and other system level parameters. This can lead to designs with unnecessarily compromised aerodynamic performance, and to "point designs," which neglect the overall mission envelope.

The absence of a comprehensive, integrated aerodynamic/aero-acoustic modeling and analysis framework represents an impediment toward achieving significant noise reduction within constraints imposed by the engine cycle, geometry, and airframe integration requirements. These gaps represent a significant opportunity to improve engineering effectiveness in the context of noise technology development for tactical aircraft. The proposed research addresses this opportunity as described below.

The overall objective of the research program summarized in this paper is to develop and demonstrate innovative methodologies for simultaneous nozzle acoustic and aerodynamic design applicable to supersonic jet exhaust noise reduction in tactical aircraft. However, only the acoustic component of the program is presented in this paper. Methodologies are being demonstrated via concept design/analysis (e.g., a chevron nozzle or non-circular geometry) followed by experimental validation at model scale. The computational efficiency and turn-around time associated with the proposed predictive tool being developed are also being addressed in order to produce robust and efficient numerical procedures that will be integrated into a design procedure and applied to nozzle geometries being developed in on-going programs on noise reduction.

The proposed effort leverages existing software tools at TTC Technologies, Inc. (TTC), as well as novel jet noise modeling and experimental diagnostic capability currently being developed under a NAVAIR-funded effort involving TTC, United Technologies Research Center (UTRC) and California Institute of Technology (Caltech). In specifics, the technical approach proposed here combines: (1) existing TTC

capability in the area of RANS/LES-CFD tools (AEROFLO software package) and fine-scale turbulence noise modeling, (2) new reduced-order unsteady modeling methods for large-scale turbulence noise under development at Caltech, and (3) experimental facilities and novel experimental diagnostic techniques available at UTRC. This combined effort is directed towards the design and performance analysis of nozzle components at the application phase beyond the current contract.

Embedded in the modeling and simulation tools is the innovative approach of designing nozzles to mitigate the large-scale structure noise which dominates the peak engine noise in the aft direction. The approach is grounded in modification of the initial flow conditions at the nozzle exit to generate/control flow instabilities, which change the evolving downstream shear layer responsible for noise generation. Identification of nozzle exit plane initial conditions with sufficient control authority to achieve downstream noise reduction while maintaining nozzle performance represents the key opportunity of the program. Currently, RANS-based computations of mean flow and turbulent kinetic energy reductions are used as a surrogate analysis procedure to determine the potential noise reduction in the absence of direct prediction methods. The proposed tool package will add acoustic analyses for the engine exhaust radiation field to allow analysis of novel nozzle configurations.

The feasibility of the proposed methodologies has been successfully demonstrated in earlier studies by the authors, which are summarized in this paper. Of primary interest is the accuracy of the simulations compared to experimental data, as well as the practicality of simulations in terms of turn-around time.

The current effort in this program focuses on the development of robust design procedures employing our earlier methodologies. Toward this objective, diagnostic experiments are employed to identify modeling deficiencies and guide model improvements. As improvements are made, the methodologies and design procedures will be employed/validated in ongoing DoD nozzle development programs.

II.   The Computational Methodology

The modeling and analysis approach is comprised of three major elements: (1) Reynolds-averaged Navier-Stokes (RANS)-CFD for computing the jet turbulent mean flow and nozzle aerodynamic performance, (2) pressure wave packet-based methods for predicting near-field sound generation from the largest scales, based on the Parabolized Stability Equations (PSE) and the aforementioned RANS solutions, and (3) a method based on the solution of the linear wave equation for determining the acoustic radiation field from the PSE solution. The proposed methodology has been demonstrated in prior work by the authors, leading to a generation 1 version (GEN1) of the prediction software tool, utilizing a linear form of the PSE methodology (LPSE). The three main elements comprising the integrated approach (Figure 1) are described below.
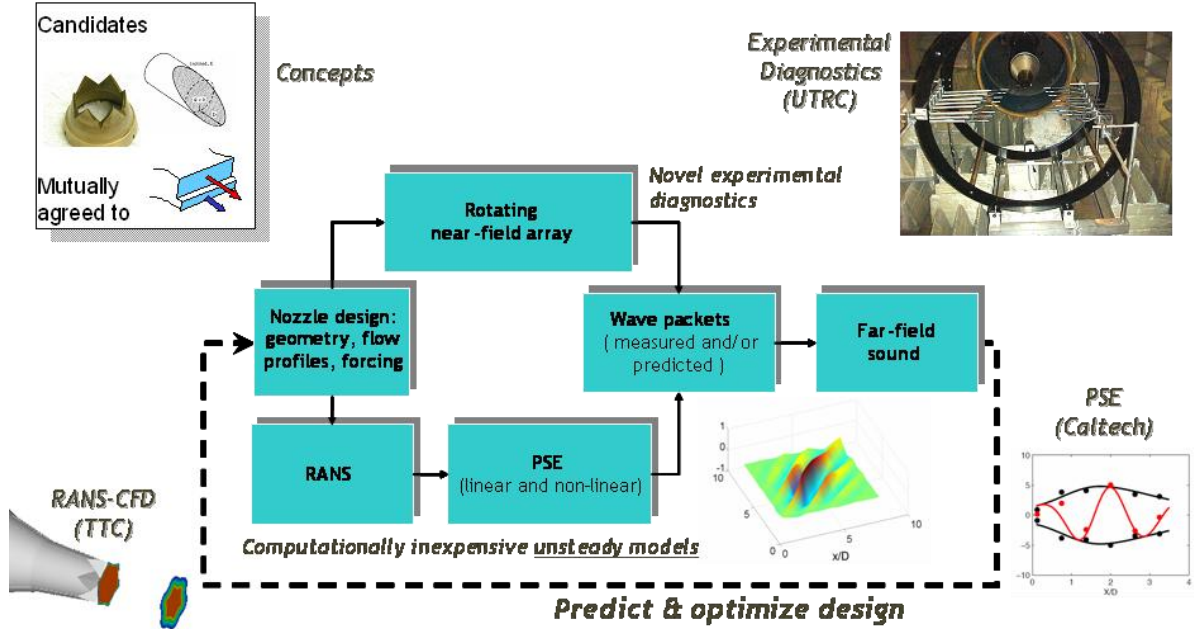
Figure 1 The nozzle acoustic/aerodynamic design procedures and team members' responsibility

III.   The RANS/LES Component of the Integrated Tool

Although TTC owns a substantially enhanced version of the finite-volume based VULCAN RANS/LES code, we have decided to use AEROFLO, also developed by TTC, as the vehicle for the implementation of the integrated tool. AEROFLO is based on high-order curvilinear, finite difference schemes, with advanced overset capability. The RANS models available in AEROFLO for generating the base flow for the PSE method include Spalart-Allmaras (SA), detached eddy simulation (DES), various versions of the k-ε, k-ω, and k-τ models, as well as the partially-resolved numerical simulation (PRNS) models that are currently being developed at NASA Glenn and TTC. The various turbulence formulas inherit the high-order accuracy of the schemes that are used for the base Navier-Stokes equations, which comprise of the compact schemes (subsonic flows) and various versions of the weighted essentially-non-oscillatory (WENO) schemes (transonic and supersonic flows). (Low-order spatial discretization with the MUSCL schemes is also supported in the tool.) The large-eddy simulation (LES) procedures in AEROFLO include the standard Smagorinsky and dynamic Smagorinsky models, Vreman's version of the Smagorinsky model, and the recent approach by Menon, which involves the solution of an evolution equation for the sub-grid scale turbulence kinetic energy. The high-order capability in AEROFLO is also very advanced, to the point that it was successfully used to calculate flow over complete Boeing 747-200 aircraft five years ago (Ladeinde et al., 2006), making it the first application of a high-order code to calculate a realistic complex geometry.

A. The Spatial Schemes in AEROFLO

The spatial schemes in the high-order procedures presented are based on the finite difference method, because of the low cost relative to other options, such as finite volume and finite elements. Shu (1997) has reported that a high-order 3D finite volume method is approximately nine times as expensive as the finite difference method. The finite element method could even be more expensive because of the numerical quadrature that is required for high-order schemes. We use the MUSCL schemes for low-order calculations and the compact and WENO schemes for high-order discretization. The compact scheme is intended for incompressible and subsonic flows, whereas WENO is used for transonic and supersonic flows. The basic forms of the schemes in AEROFLO are summarized below.

4

1. MUSCL

This simple, fairly robust, low-order scheme that uses Roe flux-splitting at the mid-point values was introduced by van Leer. First, the left and right values of the primitive variables at mid-point between two nodes are computed as

$$\phi_{i+\frac{1}{2},L} = \phi_i + \beta_i \quad \text{and} \tag{1}$$

$$\phi_{i+\frac{1}{2},R} = \phi_{i+1} - \beta_{i+1} \tag{2}$$

where $\phi = (\rho, u, v, w, p)^{\mathrm{T}}$ is the vector of primitive variables and β_i is the "limited slope" at point *i*. Here, *p* is the thermodynamic pressure. The limited slopes β_i are computed using van Leer's harmonic limiter.

Based on the left and right states at *i+1/2*, the numerical flux is computed using Roe flux-splitting as

$$\hat{F}_{i+\frac{1}{2}} = \frac{1}{2}\left(\hat{F}_{i+\frac{1}{2},L} + \hat{F}_{i+\frac{1}{2},R} - |A|\left(\left(\frac{Q}{J}\right)_R - \left(\frac{Q}{J}\right)_L\right)\right). \tag{3}$$

Here, the "*R*" and "*L*" values are constructed using the corresponding values of the primitive variables. Matrix $|A|$ is constructed using the Roe-averaged state at *i+1/2*:

$$|A| = R_{Roe}|\Lambda_{Roe}|R_{Roe}^{-1}, \tag{4}$$

where $|\Lambda|$ is the diagonal matrix of the absolute eigenvalues of the Jacobian, $\partial\hat{F}/\partial Q$.

2. Compact

The Padé method is used to approximate the spatial derivatives for subsonic flows. Consider the differencing of a variable ϕ (e.g., a conserved variable, a flux component, etc.) along the ξ-direction, or $\phi' = \partial\phi/\partial\xi$. An implicit, centered finite difference formula is employed to calculate the numerical values ϕ_i':

$$\alpha\phi_{i-1}' + \phi_i' + \alpha\phi_{i+1}' = b\frac{\phi_{i+2} - \phi_{i-2}}{4\Delta\xi} + a\frac{\phi_{i+1} - \phi_{i-1}}{2\Delta\xi}. \tag{5}$$

The parameters α, *a*, and *b* determine the spatial accuracy of the algorithm. Their values are determined from a Taylor series expansion around point "*i*." For a sixth-order accurate scheme, $(\alpha, a, b) = \left(\frac{1}{3}, \frac{14}{9}, \frac{1}{9}\right)$.

Compact finite differences are non-dissipative and are therefore susceptible to the numerical instabilities that are due to flow nonlinearities. In order to enforce numerical stability, a low-pass filtering procedure is adopted. For a typical component of the solution vector, ϕ, the filtered values $\tilde{\phi}$ are obtained from

$$\alpha_f\tilde{\phi}_{i-1} + \tilde{\phi}_i + \alpha_f\tilde{\phi}_{i+1} = \sum_{k=0}^{N}\frac{a_k}{2}\left(\phi_{i+k} + \phi_{i-k}\right). \tag{6}$$

The coefficients a_k are expressed in terms of the parameter α_f, which controls the strength of the filter, and, as it is reduced, a wider band of high frequencies is damped. A range $0.3 \le \alpha_f < 0.5$ is suggested.

3. WENO

For high-order differencing of flow fields with shock waves, the characteristic-wise WENO procedure is used (see Shu (1997), procedure 2.10). This numerical approach is summarized below.

Considering the ξ-direction as an example, we have

$$\left.\frac{\partial\hat{F}}{\partial\xi}\right|_i = \frac{1}{\Delta\xi}\left\{\left[\tilde{R}_{Roe}\cdot\left(\tilde{R}_{Roe}^{-1}\cdot\hat{F}\right)\right]_{i+\frac{1}{2}} - \left[\tilde{R}_{Roe}\cdot\left(\tilde{R}_{Roe}^{-1}\cdot\hat{F}\right)\right]_{i-\frac{1}{2}}\right\}, \tag{7}$$

where $\tilde{R}_{Roe}$ is the matrix formed with the right eigenvectors of the Jacobian $\partial\hat{F}/\partial Q$ computed based on a Roe-averaged state at *i±1/2*. For the characteristic-wise WENO, the reconstruction procedure is performed

on the characteristic fields $\hat{F}_c = \tilde{R}_{Roe}^{-1} \cdot \hat{F}$ to obtain the values at $i+1/2$. The Lax-Friedrichs flux-splitting method is used to obtain the left and right states at the mid-points:

$$\hat{F}_c^{\pm} = \frac{1}{2}\left(\hat{F}_c \pm \alpha q\right),$$ (8)

where α is the spectral radius of the Jacobian $\partial\hat{F}\big/\partial Q$. The characteristic-wise fluxes at the mid-points are reconstructed as

$$\hat{F}_{c,i+\frac{1}{2}}^{+} = \sum_{r=0}^{k-1} \omega_r F_{c,i+\frac{1}{2}}^{(r)+}, \quad \hat{F}_{c,i+\frac{1}{2}}^{-} = \sum_{r=0}^{k-1} \tilde{\omega}_r F_{c,i+\frac{1}{2}}^{(r)-}, \quad F_{c,i+\frac{1}{2}}^{(r)} = \sum_{m=0}^{k-1} c_{rm} \hat{F}_{c,i-r+m},$$ (9)

where ω_r and $\tilde{\omega}_r$ are normalized weights, based on smoothness indicators of the numerical fluxes, and c_{rm} are the coefficients for the Lagrange interpolation. Finally, the reconstructed characteristic fluxes are converted back to physical space, $\hat{F}_{i+\frac{1}{2}}^{\pm} = \tilde{R}_{Roe} \cdot \hat{F}_{c,i+\frac{1}{2}}^{\pm}$, and the numerical flux formed as

$$\hat{F}_{i+\frac{1}{2}} = \hat{F}_{i+\frac{1}{2}}^{+} + \hat{F}_{i+\frac{1}{2}}^{-}.$$ (10)

The viscous fluxes are discretized with explicit second-order finite differences when the MUSCL scheme is used for the convective fluxes, and with high-order finite differences, when the compact (sixth-order) or WENO (fifth-order) schemes are used for the convective fluxes.

4. Newer WENO Schemes in AEROFLO

Newer versions of the WENO schemes have recently been implemented in AEROFLO to allow for a more consistent superior performance for a wide range of problems. This includes the WENO-M and the WENO-Z schemes.

The WENO-M Smoothener
This procedure modifies the weights to mitigate the quick degeneration of the WENO scheme to lower order accuracy in the vicinity of (even) the weakest discontinuities. This is because the weights used by Jiang and Shu (1998) (hereafter referred to as JS) are very sensitive and quickly nullify the contribution of a "heavy" stencil, hence reducing the scheme to just two stencils with an approximate third-order performance. The modified weights can be written as

$$\tilde{w}_k = \frac{\gamma_k}{(\varepsilon + \beta_k)^p},$$ (11)

where the optimal weights γ_0, γ_1, and γ_2 are given as 0.1, 0.6, and 0.3, respectively, ε is a small, non-zero number introduced in order avoid division by zero when the smoothness indicators have zero values. The parameter p is usually taken as 2, following the procedure of JS. The weights are modified using smoothness indicators β_k, such that the contributions from stencils with large variations are minimized, while those from stencils in smooth regions are made to approach the optimal values. Finally, the modified weights are renormalized:

$$w_j = \frac{\tilde{w}_j}{\sum_{k=0}^{2} \tilde{w}_k}.$$ (12)

In WENO-M, these weights are further modified or remapped as follows (Henrick et al., 2005):

$$g_k = \frac{w_k\left(\gamma_k + \gamma_k^2 - 3\gamma_k w_k + w_k^2\right)}{\gamma_k^2 + w_k\left(1 - 2\gamma_k\right)}$$ (13)

The recomputed weights are then normalized again to obtain remapped weights:

$$w_j = \frac{g_k}{\sum_{k=0}^{2} g_k} \, , \tag{14}$$

which are then used in the computation of the fluxes. An additional modification applied to reduce the sensitivity of the smoothener was to set $p = 1$.

C.2. The WENO-Z Smoothener
This procedure also modifies the weights, but in a much simplified manner that leads to much fewer arithmetic operations. Thus, WENO-Z is significantly faster than WENO-M, with a comparable level of accuracy. The modification to the smoothener, and therefore weights, is as follows (Jacobs et al., 2008; Borges et al., 2008):

$p = 1$

$$\tau_2 = |\beta_0 - \beta_2|$$
$$\tilde{\beta}_k = \left(1 + \frac{\tau_2}{\beta_k + \varepsilon}\right) \tag{15}$$

$p = 2$

$$\varsigma_2 = (\beta_0 - \beta_2)^2$$
$$\tilde{\beta}_k = \left(1 + \frac{\varsigma_2}{(\beta_k + \varepsilon)^2}\right) \tag{16}$$

B. Time Integration

Several time-marching schemes are supported in AEROFLO. For problems where accurate time-dependent solutions are required, the classical fourth-order Runge-Kutta (RK4) scheme is employed in its low-storage form. Because of its relatively severe stability constraint, RK4 is inappropriate for flow problems in which only the steady state solutions are sought. The approximate factorization procedure of Beam and Warming, with the diagonalized simplification by Pulliam and Chaussee (1981), is employed for these cases:

$$\left[\left(J^{-1}\right)^{(p+1)} + \frac{1}{1+\varphi} dt \delta_\xi \left(\frac{\partial \hat{F}^{(p)}}{\partial Q} - \frac{\partial \hat{F}_v^{(p)}}{\partial Q}\right)\right] J^{(p+1)} \times$$

$$\left[\left(J^{-1}\right)^{(p+1)} + \frac{1}{1+\varphi} dt \delta_\eta \left(\frac{\partial \hat{G}^{(p)}}{\partial Q} - \frac{\partial \hat{G}_v^{(p)}}{\partial Q}\right)\right] J^{(p+1)} \times$$

$$\left[\left(J^{-1}\right)^{(p+1)} + \frac{1}{1+\varphi} dt \delta_\zeta \left(\frac{\partial \hat{H}^{(p)}}{\partial Q} - \frac{\partial \hat{H}_v^{(p)}}{\partial Q}\right)\right] \Delta Q \tag{17}$$

$$= -\frac{dt}{1+\varphi}\left[\left(J^{-1}\right)^{(p+1)} \frac{(1+\varphi)Q^{(p)} - (1+2\varphi)Q^{(n)} + \varphi Q^{(n-1)}}{dt} + \delta_\xi\left(\hat{F}^{(p)} - \hat{F}_v^{(p)}\right) + \delta_\xi\left(\hat{G}^{(p)} - \hat{G}_v^{(p)}\right) + \delta_\zeta\left(\hat{H}^{(p)} - \hat{H}_v^{(p)}\right)\right]$$

where $\varphi = 1/2$ yields a three-point backward stencil in time. Here, derivatives δ_i are obtained with standard second-order centered differences in the implicit operators on the left-hand side, while the right-hand side differences are computed using the high- and low-order spatial schemes described above. In order to reduce the errors associated with the approximate factorization and diagonalization procedures, Newton-like sub-iterations are performed. Note that in the equation above, the superscript "n" denotes the iteration number, and superscript "p", the sub-iteration count. Within one iteration, $Q^{(p)} = Q^{(n)}$ and, at convergence in p, $Q^{(n+1)} = Q^{(p)}$. Typically three sub-iterations are applied per time step. Our code also supports a third-order total-variation-diminishing (TVD) Runge-Kutta time integration procedure.

C. The Accuracy of AEROFLO

We employed the Method of Manufactured Solutions (MMS) to demonstrate the high-order accuracy of AEROFLO and compare the accuracy to the theoretical values. The results in Figure 2 were an outcome of the investigation, wherein the accuracy observed for a manufactured problem using the MUSCL (low-order), compact (high-order, subsonic), and WENO (high-order, supersonic/hypersonic) are shown. Note that the observed accuracy depends on the boundary conditions, as illustrated in the figure for compact schemes ((C_4C_6) shows lower accuracy compared to (C_5C_6)), and that the use of component-wise or characteristic-wise procedures in WENO did not significantly alter the accuracy.
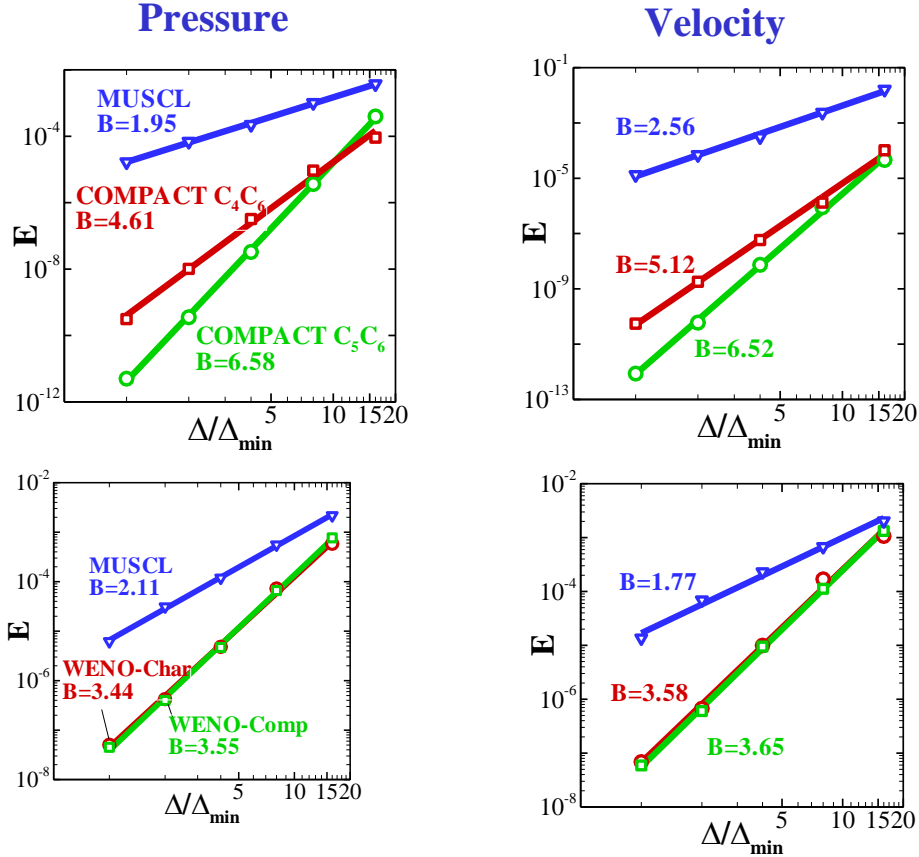
Figure 2 Validation of the high-order accuracy of AEROFLO for subsonic flow (compact, top row) and supersonic flow (WENO, bottom row) using the Method of Manufactured Solutions (MMS). MUSCL is applicable at all speeds. The theoretical accuracy is second-order (MUSCL), sixth-order (compact), and fifth-order (WENO).

D. Validation of AEROFLO for Jet Noise Simulation

Numerous studies have been carried out at TTC to validate the accuracy of AEROFLO for jet noise prediction. The studies started with the investigation of the performance of the large-eddy simulation module, with a focus on the large-scale structures, which are known to generate most of the aft noise. Since the phenomenon resides in the large scales, it appears that a relatively coarse-grid LES should be appropriate. We set out to investigate this hypothesis under a task we termed "very large-scale eddy simulation," or VLES, for short. We also carried out simulations based on RANS and hybrid RANS/LES. A typical grid topology used in our studies is shown in Figure 3, with Figure 3(b) showing a close-up view of the nozzle exit region. As shown in the figure caption, the number of grid points is usually less than two million for either the RANS or RANS/LES. It is important to stress that the LES procedures in AEROFLO

8

are based on the most advanced procedures in the open literature, even if we choose to use coarse grid models within our VLES framework.

a)   Sample grid topology used for RANS/LES simulations, b) close-up of the nozzle exit region
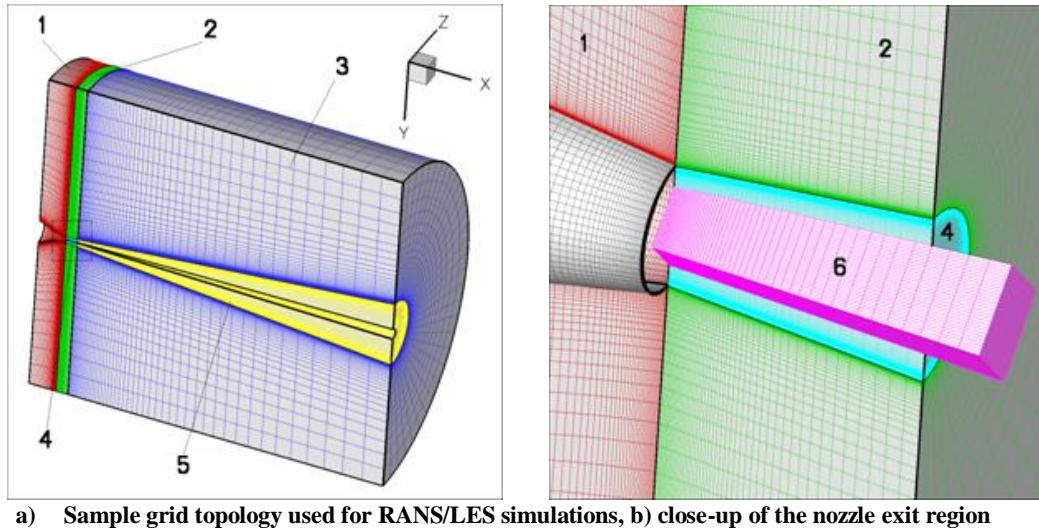
Figure 3 Computational overset grids in our VLES and RANS studies of jet noise prediction, showing a) a sample block topology and b) a close-up on the nozzle exit region. In all studies, RANS is used to calculate the flow inside the nozzle, whereas either VLES or RANS is used in the plume region. A typical VLES grid has 1,731,564 points (including the nozzle interior flow), whereas the grids for the RANS calculations are usually around 1,323,518 points.
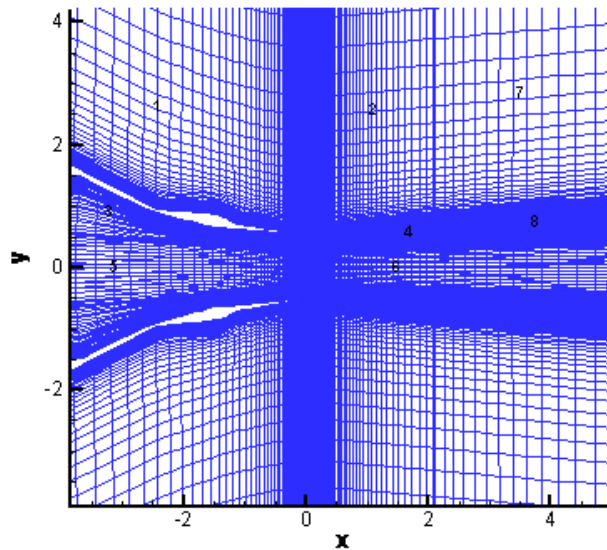
Figure 4 Grid distribution in the vicinity of the nozzle exit

Figure 4 is a two-dimensional slice that shows the grid details in the vicinity of the nozzle exit, while Figure 5 shows two mesh systems in the vicinity of the centerline. Although both are overset, Figure 5(a) shows a more powerful (overset) gridding system involving overlapping and non-conforming grid topology at the center region.
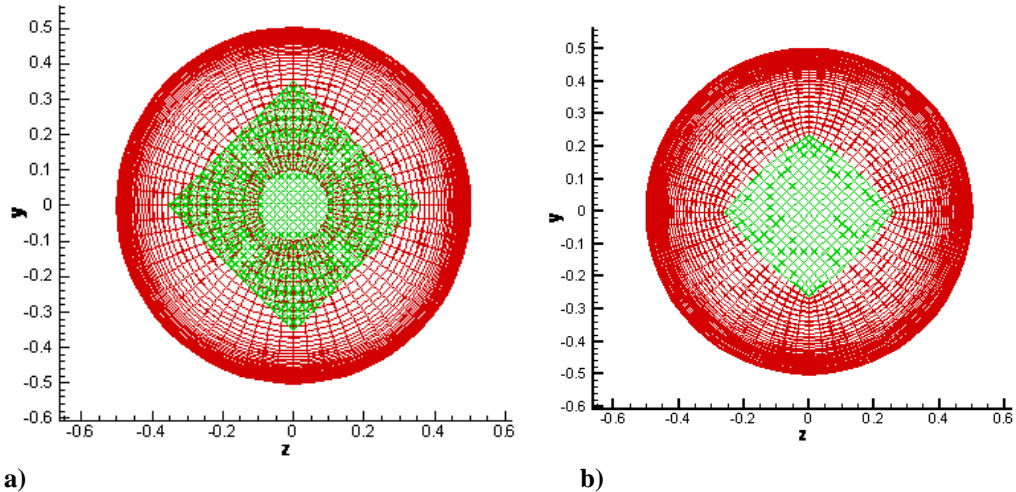
Figure 5 Two overset mesh systems to handle centerline singularity; a) overlapping, non-conforming, b) non-overlapping, conforming system

Simulations using LES have been carried out for many cases for which experimental data were available in the literature, such as Tanna's round jet Set Point 46 (SP46) (hot) and Tanna's round jet Set Point 7 (SP7) (cold). In many other cases, the experimental data were generated within the team, via the facilities at UTRC. Figure 6 shows a VLES/RANS simulation of SP7. The general large-scale features of the appear to have been captured.
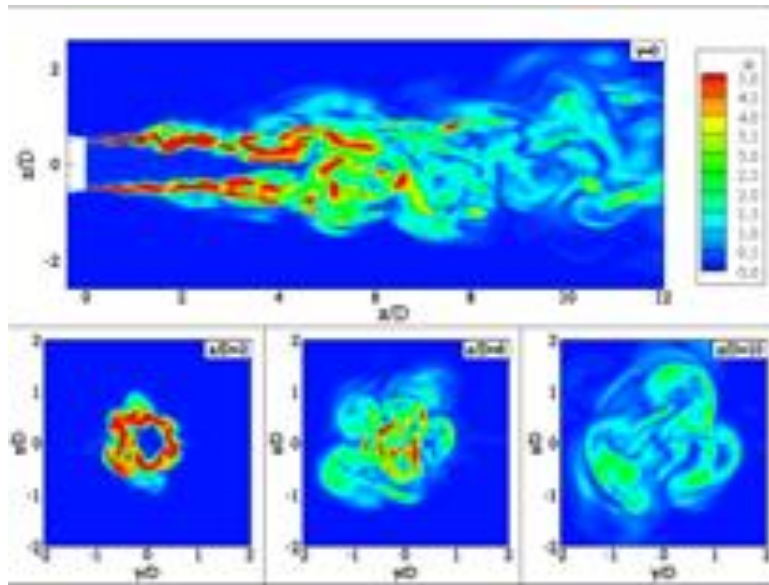
Figure 6 VLES Simulation of Tanna's round jet Set Point 7 (SP7), showing the axial development and transverse cuts. Note that in all our studies, RANS is used to calculate the flow inside the nozzle.

The same problems were also calculated using RANS in the plume region (i.e., RANS/RANS), with a comparison of the results with Bodony and Lele (2006) and Tanna's experimental data (Figure 7). These results show a superior performance of RANS/RANS (over RANS/VLES) for the prediction of the normalized axial jet velocity. The radial distribution of the axial velocity component and the *rms* of the axial fluctuating velocity component (Figure 7(c)) show excellent agreement with the experimental data for both variables. Note that the Witze correlation has been used to scale the axial distance by the potential core length. Two-point correlation blind tests of AEROFLO predictions against experimental data measured at UTRC, are shown in Figure 8, while Figure 9 shows the power spectral density (PSD).
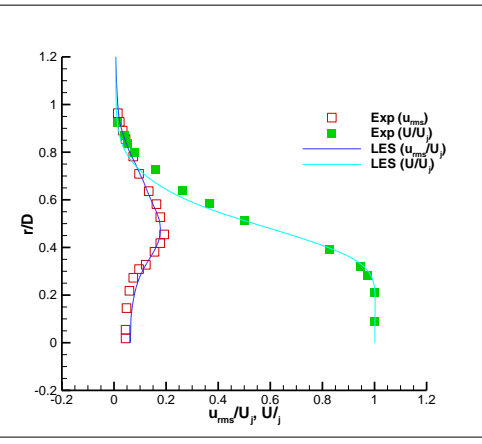
10

a)

b)

c)
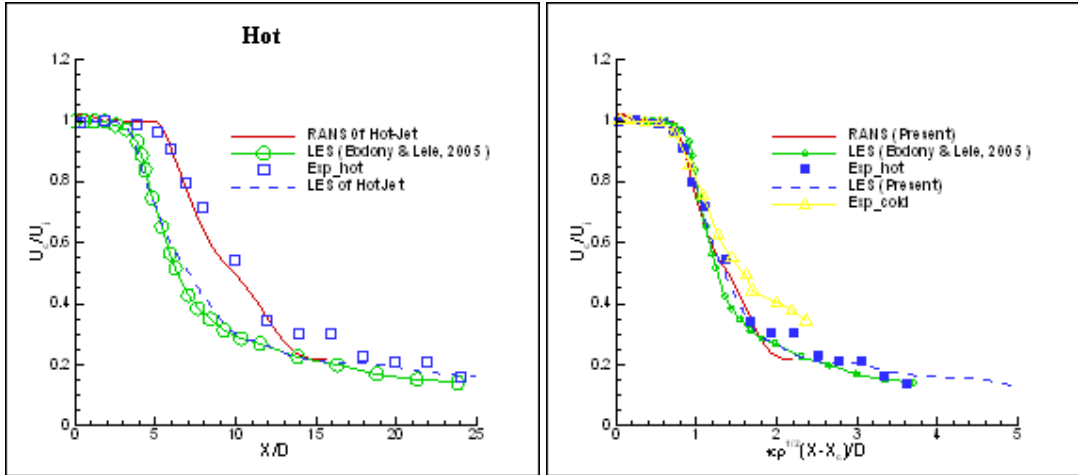
Figure 7 VLES/RANS and RANS/RANS simulation of Tanna's round jet (SP46 and SP7), showing comparison with Bodony and Lele (2006) and Tanna's experimental data. (a): hot jet, (b): hot and cold jet, (c): cold jet. Figure 7(c) is adjusted for the potential core length. Figure 7(a) shows that our RANS/RANS is more accurate than our VLES and the VLES by Bodony and Lele (2006).
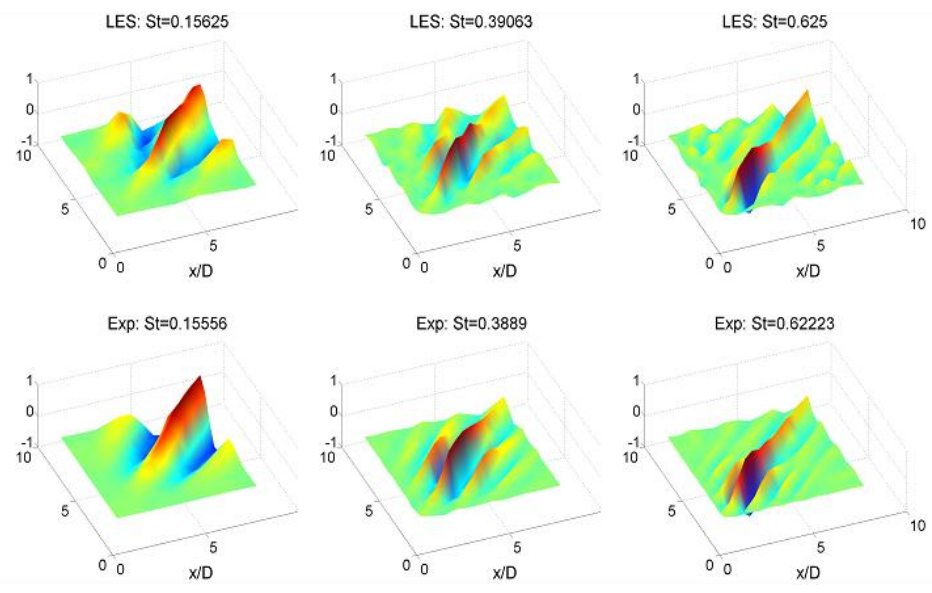

Figure 8 Real part of the two-point correlation function *Rm* as function of *x1* and *x2* for Tanna SP7. VLES (top) compared to experiment (bottom); *m*=0; *St* = .16, .31, .39. The raw data are from Colonius and Suzuki (2006). AEROFLO RANS/VLES results for other modes, m=1, m=2 (not shown) are equally promising, even for the level of refinement. All tests were blind, meaning that TTC did not

11

know the results and AEROFLO output data were post-processed at UTRC where the experimental data were collected.
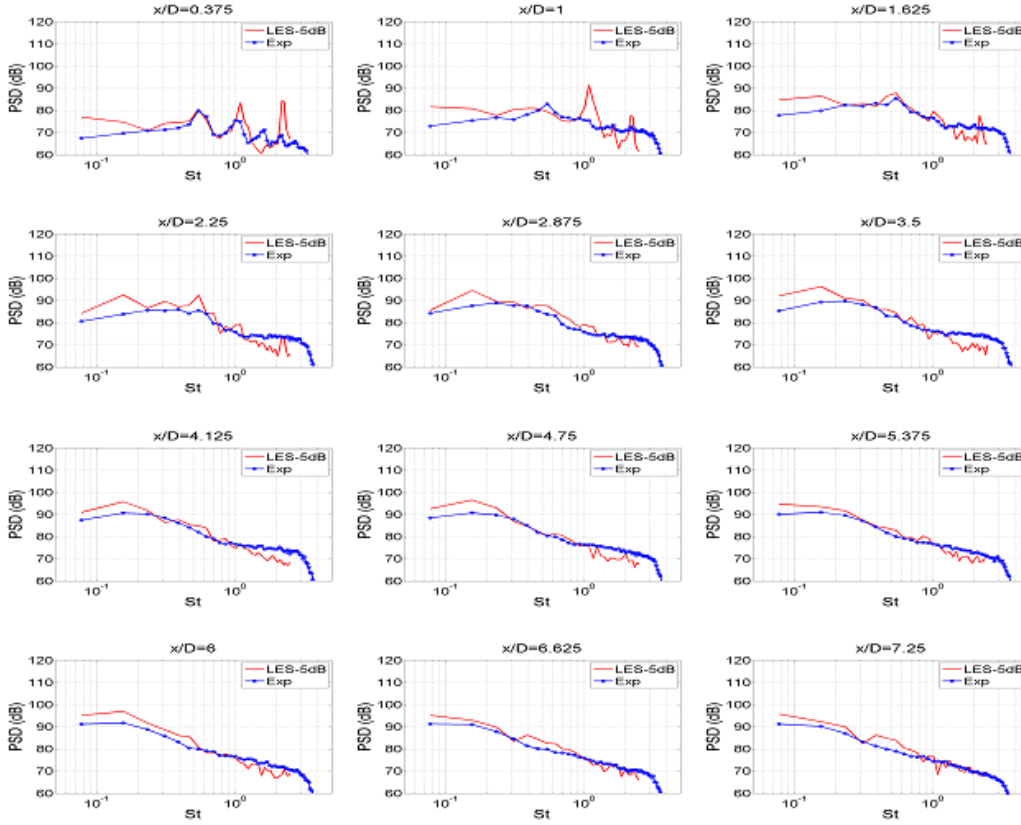
Figure 9 Comparison of measured and simulated pressure spectra along hydrodynamic array for Tanna Sp 7; *m*=1; Δ*St* = .0196. The raw data are from Colonius and Suzuki. LES results have been shifted by –5 dB. All tests were blind, meaning that TTC did not know the results and AEROFLO data were post-processed at UTRC where the experimental data were collected.

The remaining discussions on AEROFLO validation below focus on RANS/RANS (i.e., RANS inside the nozzle and RANS in the plume). The purpose of Figure 10 is to show the relative performance of RANS modeling using Spalart-Allmaras (SA) and the k- ε models, using SP7 and Set Point 3 (SP3) for the tests. SA is of interest because it is cheaper to calculate and thus would be preferred if the procedure leads to an accurate prediction. Unfortunately, the poor performance of SA is evident in Figure 10. Thus, although the RANS mean flow calculations for PSE were initially carried out with SA, we switched to k-ε after realizing the poor performance of the former approach.
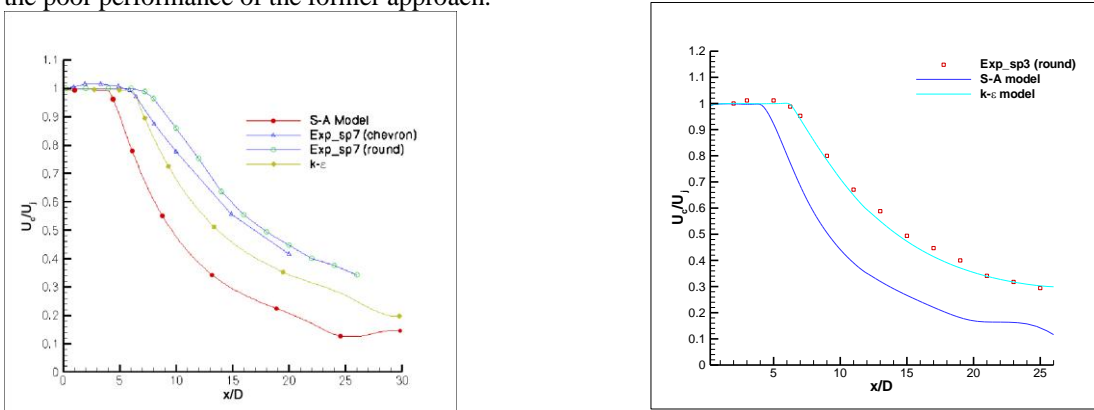
Figure 10 Comparison of Spalart-Allmaras and k-ε models

12

for SP7 and SP3. The poor performance of SA is evident.

Figure 11 compares AEROFLO RANS predictions of chevron nozzle (SMC001) flow with experimental data using the SP7 conditions. Although this comparison is qualitative, the performance of AEROFLO appears excellent.
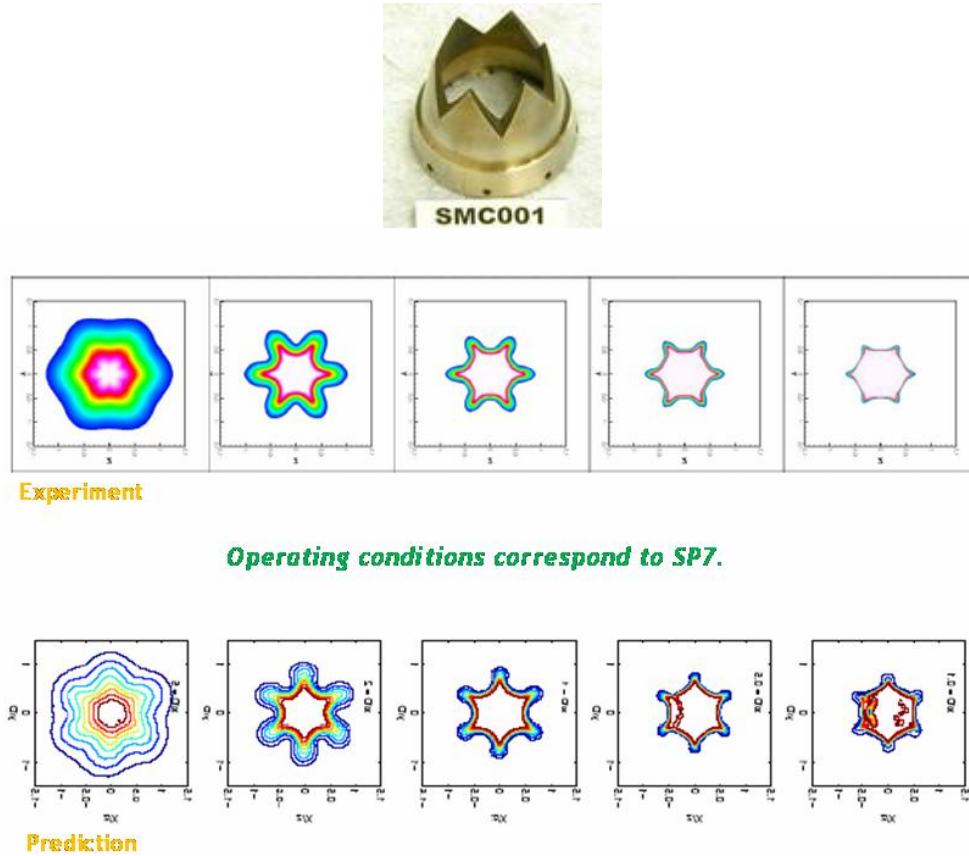

**Figure 11 Comparison of AEROFLO predictions with
PIV data for subsonic Chevron nozzles, using the SP7 data**

We will conclude the discussions on AEROFLO validation for the integrated tool by considering supersonic, perfectly expanded, Mach 1.5 nozzles. For this purpose, we consider the conditions for B118, B120, and B122 (Table 1). Note that B118 involves a round nozzle, with cold jet, whereas B120 involves a round nozzle, with a hot jet. B122 has a chevron nozzle and the jet is hot. These three configurations have been analyzed using each of the three components of the integrated reduced-order tool (RANS, PSE, and wave-packet). For the RANS part, only B118 and B122 will be discussed in this paper.

Set pt.	M_∞ (M_{jet})	T_{jet}/T_∞
$B118$	1.50 (1.5)	1.00 (cold)
$B120$	1.77 (1.5)	1.40 (hot)
$B122$	1.98 (1.5)	1.74 (hot)

Table 1 Perfectly-expanded supersonic test cases

In an exploratory RANS calculation of B118, the interest arose to do calculations without including the nozzle, and compare the results with cases where the nozzle is included. We wanted to determine the cause of the abrupt drop in the mean axial velocity profile at the end of the potential core that was observed for cases where the nozzle is excluded from the model. For this case, imposing a turbulence field at the nozzle exit did not solve the problem with the abrupt decay; neither did judicious mesh refinement. The turbulence

decayed very quickly as the flow moves away from the exit. It was interesting to observe that the inclusion of the nozzle geometry as part of the model removed the abrupt decay. Figure 12(a) shows the RANS results for B118, with and without the nozzle in the model. The most prominent difference is the abrupt decay alluded to above. Note that the number of grid points for the simulations are 1,025,340 (with and without nozzle), 650,000 (without nozzle). For B122, only one chevron is modeled, with a grid of 804,555 points.

a)   b)
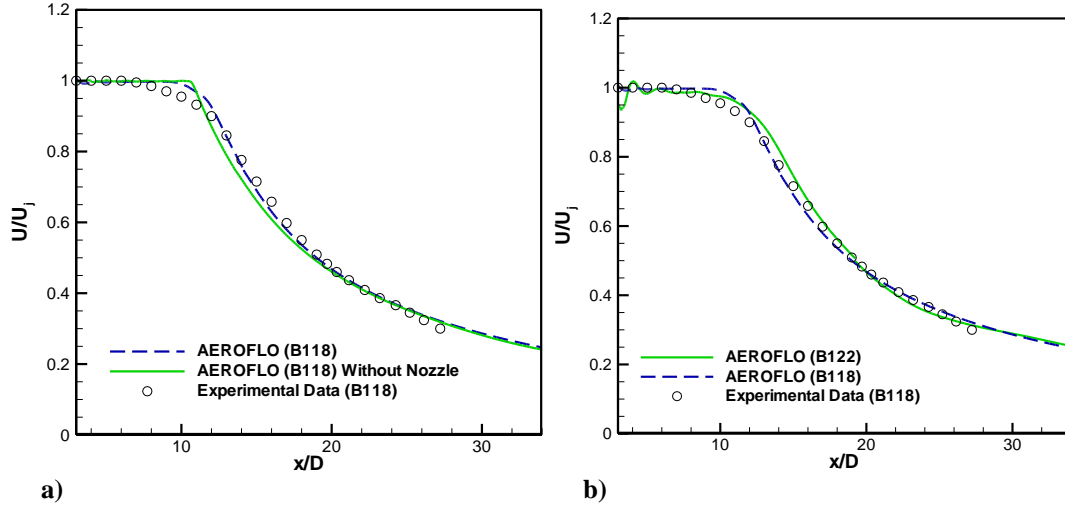
Figure 12 Evaluation AEROFLO RANS for B118 and B122: (a) B118 results, with and without the nozzle in the model., (b): B118 and B122, both with nozzle included.
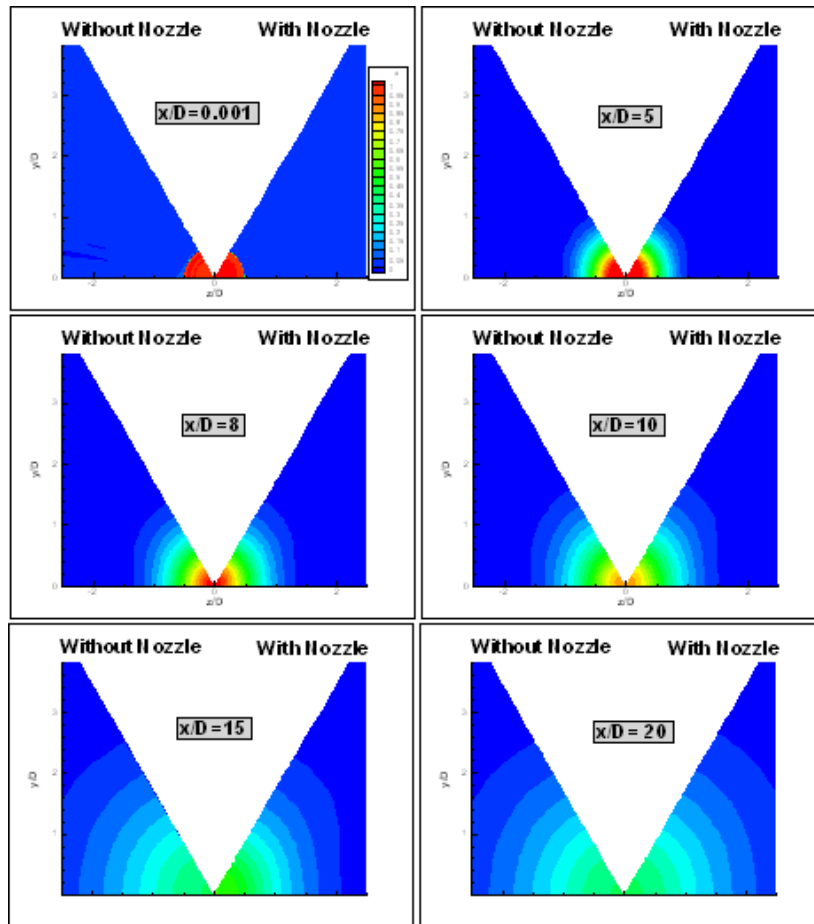

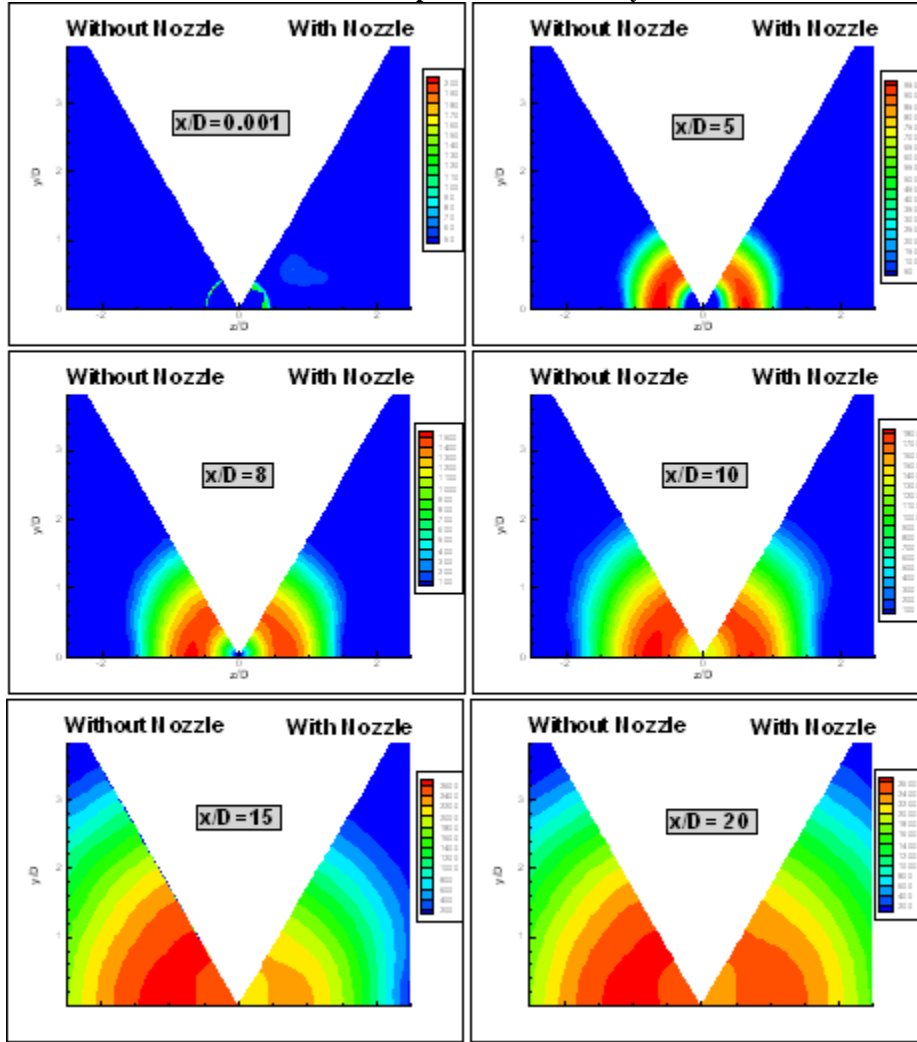**Figure 13 Details of B118 flow at selected axial locations, with and without**

14

Figure 14 Details of B118 flow at selected axial locations, with and without the nozzle. Contour maps of the eddy viscosity distribution are shown.

The details of the flow in B118 are shown in Figures 13 (axial velocity) and 14 (eddy viscosity). The results show that the presence of a nozzle appears to introduce a slight asymmetry in the flow. Note that periodic conditions are imposed in the azimuthal direction. Figure 15 below shows snapshots of the flow in the chevron of case B122 at selected axial locations. The profiles appear to be very reasonable, and are not significantly dissipated.

E. Aero performance validation of AEROFLO

To demonstrate the feasibility of the RANS capability in AEROFLO for complex nozzle aerodynamic performance analysis, mutually agreed to government test cases were to be used. However, non-proprietary data was not available so the team was tasked with identifying a viable data set. In keeping with the demonstration of the TTC RANS tool on complex chevron nozzle geometries, UTRC conducted a search for a mutually agreeable chevron data set. Figure 16 shows a baseline and 12 chevron model scale nozzle for which the discharge coefficient (C_d) and thrust coefficient (C_{tr}) were documented in an unpublished report. Model assembly with chevron nozzle is shown in Figure 17. The geometry was forwarded to TTC while the experimental results were held by UTRC to provide a blind test of the performance prediction accuracy. To retain the blind test case status for future evaluations in other studies, the measured C_d and C_{tr} values are not reported here. Rather, the deltas between predicted and measured

results are reported. Details of the geometry and test results were, however, shared with the contract monitor to obtain government concurrence.
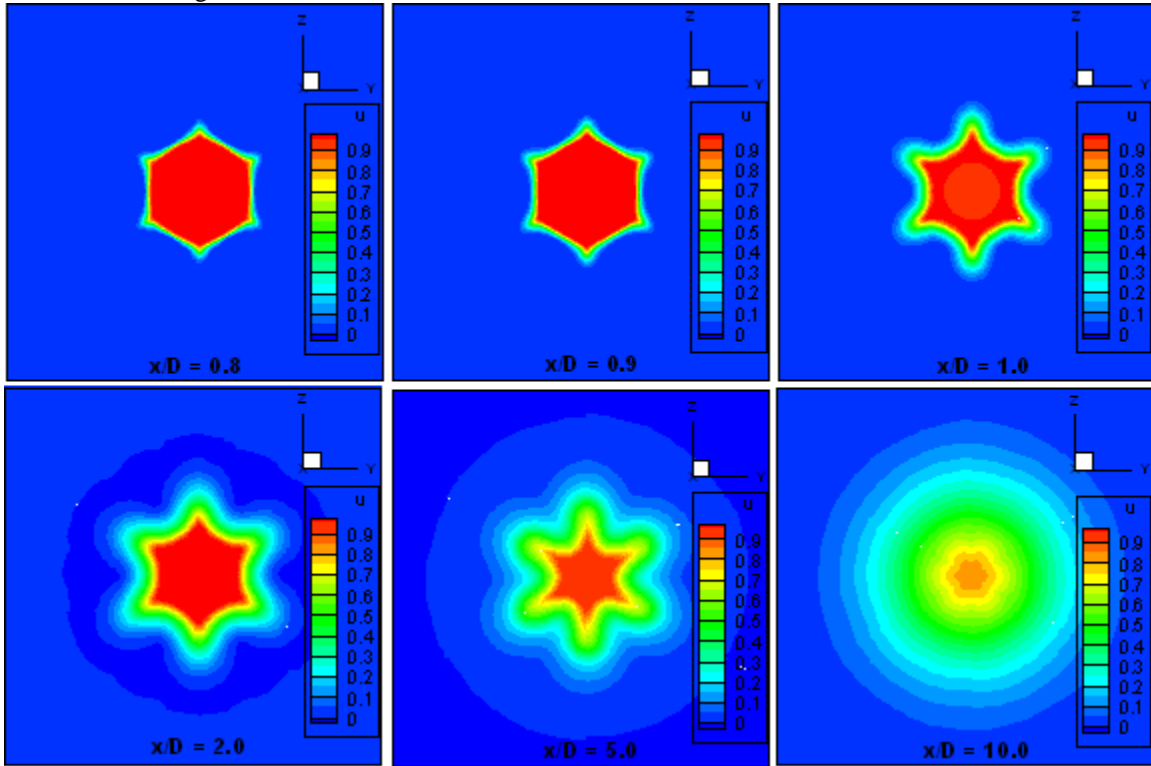

Figure 15 Axial velocity maps at selected axial locations (B122)

Internal details of the model assembly and nozzle are shown in engineering drawing of Figure 17 illustrating the complexity of the geometry which was gridded for the CFD prediction. The 12 chevrons were deflected inward in this converging nozzle design. The secondary nozzle cooling duct shown in the drawing was not included in the performance testing of the nozzle. The overall baseline and chevron nozzle pressure ratios (λ) were 2.0025, which is slightly larger than the critical pressure ratio $((\gamma+1)/2)^{\gamma/(\gamma-1)} = 1.89293$. Therefore, the nozzle flow was slightly under-expanded. Both the Spalart-Allmaras and k-ε turbulence models were evaluated, although results reported here are confined to the latter, as this model was determined to provide more accurate predictions. The calculated discharge coefficient (C_d) and thrust coefficient (C_{tr}) are presented in Table 2 as deltas relative to the
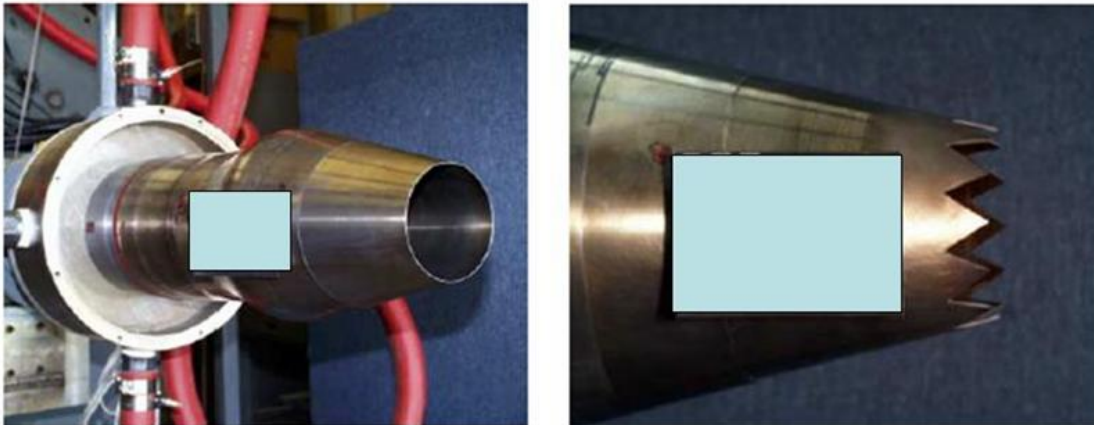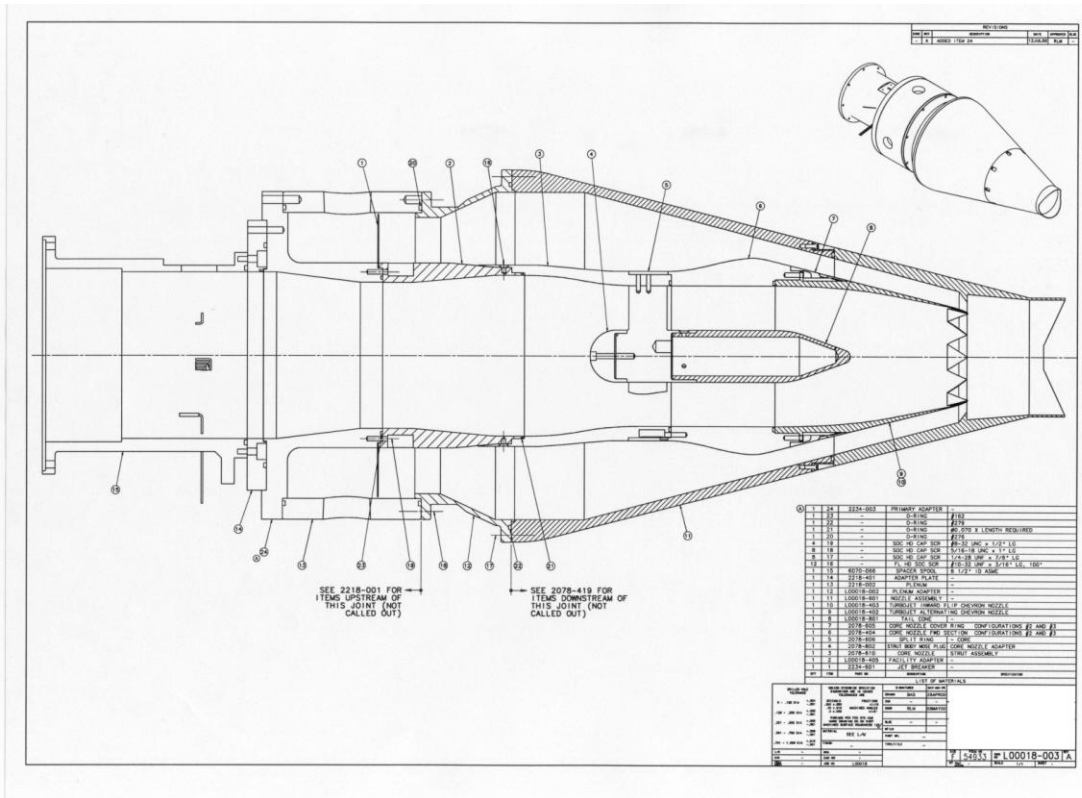

Figure 16 Baseline round nozzle and chevron nozzle with short internal plug (not visible).

16

Figure 17 Model assembly with chevron nozzle

experimentally determined values for the chevron nozzle in Figure 16. The results show a 1.5% under-prediction of C_d and a 1% over-prediction of C_{tr}.

	Delta relative to measured discharge coefficient (C_d)	Delta relative to measured thrust coefficient (C_{tr})
k-ε model	+0.0155	-0.0107

Table 2 Aero performance evaluation of AEROFLO/RANS

Fractional error relative to experimental data are shown in Table 2. It is noted that the reference scales for the RANS calculation is selected as the nozzle exit flow values under perfectly-expanded conditions: U_{ref}=326 (m/s), ρ_{ref}=1.468 (kg/m^3), p_{ref}=1/γM_j^2.

IV. The PSE Component of the Integrated Tool

The PSE method relies on predicting, as a function of frequency, the convecting pressure *wave packet* that is observed to exist in a region adjacent to the fully turbulent shear layers. This region is defined as sufficiently far from the shear layers so that mean shear is negligible and disturbance levels are sufficiently low that linearized equations suffice to describe the flow, but sufficiently close such that, for subsonically convecting disturbances, the pressure field is

Figure 18 78 microphone near-field array, constructed and tested at NASA Glenn Research center by J. Bridges and S.-S. Lee. See [5] for further details.

evanescent, or exponentially decaying, with a convective rather than acoustic phase speed. Provided that pressure fluctuations from smaller-scale turbulence in the shear layer decay sufficiently fast, the existence of such an evanescent wave region is predicted from quasi-parallel stability theory of jet mean flow fields, and was recently confirmed in detail through the use of a caged 78 microphone array (Figure 18) for a variety of jet operating points and from both round and chevron nozzles (Suzuki & Colonius, 2006). At supersonic convection velocities there is direct radiation from these wave packets in the form of Mach waves (Tam & Burton, 1984), but the overall structure of the wave packet is not qualitatively different from subsonic convection velocities.

For many years, researchers have associated large-scale turbulent structures in free shear layers with instability waves of laminar and turbulent mean flow fields (see for example, Liu, 1974; Michalke & Fuchs, 1975). Such linear stability waves exhibit the structure of convecting wave packets just outside the shear layer. However, prior attempts to model features of jet mixing and noise radiation from these models have for the most part failed, except when jets are strongly forced at frequencies for which these waves are strongly amplified by the flow. Another exception is at supersonic jet speeds, where features of Mach wave radiation have successfully been predicted and measured based directly on a Matched Asymptotic Expansion between the quasi-parallel near-field instability wave and solutions of the wave equation in the far-field (Tam & Burton, 1984). A key difference between the current approach and previous work is that we avoid attempting to *equate* measured flow quantities inside the turbulent flow with instability waves. Any such identification is problematic, since inside the region of intense turbulence, a variety of scales of motion contribute to the local pressure or velocity. On the other hand, outside the shear layer where smaller-scale pressure fluctuations are absent, it appears that the observed pressure wave-packet structure can, at least before the end of the potential core, be directly associated with linear instability waves (of the turbulent mean flow field).

The evidence for this was provided by Suzuki and Colonius (2006), where instability wave amplitudes were computed for the experimentally determined mean flow fields (from PIV measurements, see Bridges & Brown, 2004) and compared directly to pressure signals from the 78 microphone array. Ryu et al. (2008) have recently provided additional comparisons between linear stability theory and LES-determined wave packets.

Originally developed by Herbert and Bertolotti (1997), the PSE method expands the domain of traditional linear stability methods by relaxing the parallel-flow assumption as well as allowing for the inclusion of non-linear terms. PSE has been used with considerable success in the prediction of convectively unstable flows such as boundary layers (Bertolotti & Herbert, 1991), jet flows (Malik & Chang, 1997) and planar mixing layers with chemistry (Day, Mansour & Reynolds, 2001). The governing equations for the PSE component of the integrated analysis tool is contained in Appendix A of this paper.

A. Mean Flow Fourier Modes from PIV and AEROFLO/RANS

The mean flow Fourier modes obtained from PIV data for Chevron were compared with those from RANS calculations for the purpose of assessing the suitability of RANS in the RANS-PSE component of the integrated procedure. Comparative evaluation of RANS models based on $k - \varepsilon$ and Spalart-Allmaras was also carried out, in order to determine the specific RANS models to be used for the studies.

The Chevron calculations pertain to Tanna's Set Point 1 (SP1), Set Point 3 (SP3) and Set Point 7 (SP7). The flow and simulation parameters are listed in Table 3. Eight blocks with a total of approximately half a million grid points were used to calculate half of a slice of Chevron, assuming symmetry of the flow.

Case	M_j	Re	NPR	$T_j/T\infty$	Y^+	N_{grid}
SP1	0.35	3.93×10^5	1.0885	1.0	1.12	440772
SP3	0.5134	6.3×10^5	1.197	0.95	1.67	440772
SP7	0.9854	1.0×10^6	1.861	0.835	2.5	440772

Table 3 Flow parameters and the numerical setups

Fourier transform in the azimuthal direction was used to extract the modes in multiples of six for a nozzle with 6 chevrons, where the Fourier transform takes the form

$$\hat{U}_m = \int \overline{U}(x,r,\theta) \cdot \exp(im \cdot \theta) d\theta. \tag{18}$$

The extracted velocity profiles were used to solve the following compressible Rayleigh equation (CRE) for linear stability analysis:

$$\frac{1}{r}\frac{\partial}{\partial r}\left(r\frac{\partial p}{\partial r}\right) - \frac{2k}{k\overline{U}-\omega}\frac{\partial \overline{U}}{\partial r}\frac{\partial p}{\partial r} - \frac{2k}{r^2(k\overline{U}-\omega)}\frac{\partial \overline{U}}{\partial \theta}\frac{\partial p}{\partial \theta} + \frac{1}{r^2}\frac{\partial^2 p}{\partial \theta^2} - \left(k^2 - \left(k\overline{U}-\omega\right)^2\right)p = 0 \cdot \tag{19}$$

With symmetry in the azimuthal direction, we can simplify Eq. (19) to

$$\frac{1}{r}\frac{\partial}{\partial r}\left(r\frac{\partial p_m}{\partial r}\right) + \sum_{n=-\infty}^{\infty}\left(F_{N_C n}\frac{d}{dr} + (m - N_C n)G_{N_C n} + H_{N_C n}\right)p_{m-N_C n} - \left(\frac{m^2}{r^2} + k^2\right)p_m = 0, \tag{20}$$

where

$$F_j = -2k\left(\frac{1}{k\overline{U}-\omega}\frac{\partial \overline{U}}{\partial r}\right)_j, \tag{21}$$

$$G_j = -\frac{2ik}{r^2}\left(\frac{1}{k\overline{U}-\omega}\frac{\partial \overline{U}}{\partial \theta}\right)_j \tag{22}$$

$$H_j = (k\overline{U}-\omega)_j^2, \tag{23}$$

and T_j denotes the jth Fourier mode of quantity T.

The Matlab-version of the PSE procedure was converted to FORTRAN and C/C++, which were the computer languages that are used for the integrated (RANS-PSE-Wave packet) code.

Figures 19 summarizes the results of the analysis, wherein the Fourier modes obtained from PIV data are compared with those from RANS mean flows, using the Spalart-Allmaras and $k-\varepsilon$ model s for both round and Chevron nozzles (only SP7 results are shown).

Consistent with observations made previously in this paper, the k-ε RANS model is less dissipative than the Spalart-Allmaras model, and gives more accurate results, using experimental data as the reference. The centerline velocity and the Fourier modes of velocity at several cross-sections are shown. The suitability of using $k-\varepsilon$ RANS-generated results as the equilibrium solutions for the linear stability analysis was thus established.

B. Validating the PSE Procedure (Experimental Mean Flow Data)

Figure 20 below shows the pressure amplitude results obtained from the PSE procedure being used in comparison with experimental measurements for a subsonic round jet (Godmundsson and Colonius, 2007). However, the mean flow field used in analysis was measured experimentally using PIV as reported in Suzuki and Colonius (2006). The figure shows the wave packet pressure amplitude obtained for a Mach 0.9 cold jet (corresponding to set-point 7 in the study by Tanna (1976)), for azimuthal wave numbers $m = 0$ and 1, and Strouhal numbers 0.15, 0.30, and 0.45. This figure includes the results of linear stability analysis (LST). Note the significant improvement offered by LPSE over LST at $St = 0.15$, particularly for $m = 0$, clearly illustrating the importance of non-parallel effects. For higher frequencies, the differences between
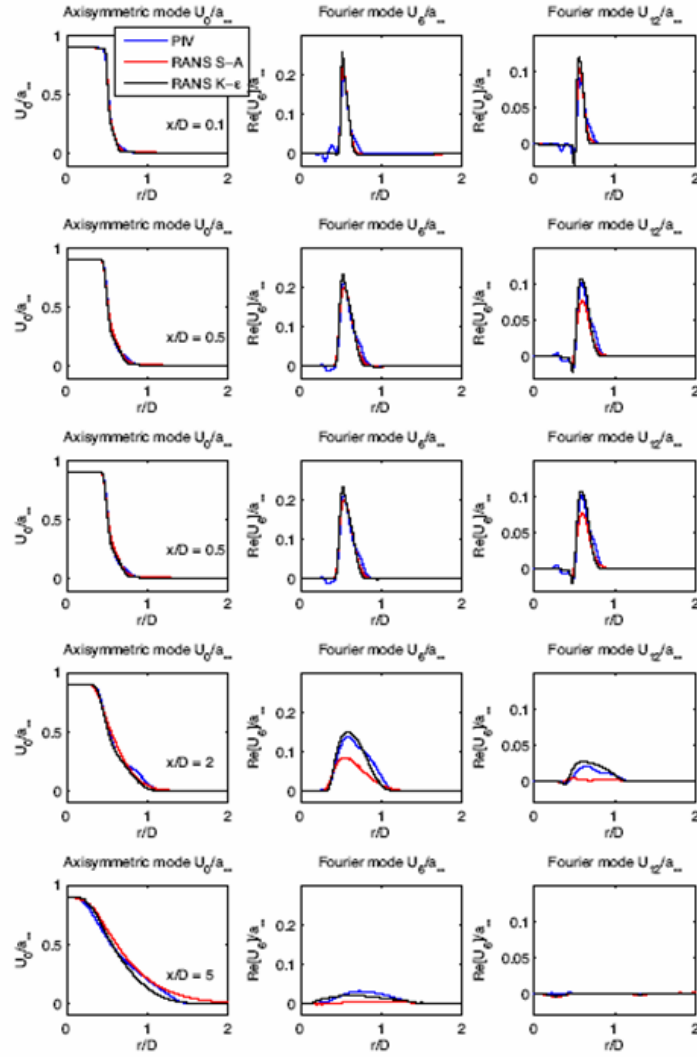
Figure 19 A comparison of (mean velocity) Fourier mode in azimuthal direction between PIV (blue line) and Spalart-Allmaras RANS (red line) and k-ε (black line) for SP7

LST and LPSE mostly disappear; at these frequencies, the disturbance wavelengths are such that non-parallel effects, the only distinction between LPSE and LST, are of vanishing importance.

C. Validating the PSE Procedure (RANS Mean Flow Data)

In order to evaluate the predictive capability of PSE for a supersonic jet, we consider a Mach 1.5 perfectly expanded cold jet (set-point B118 in Tanna, Dean, and Burrin (1976)), which was measured in a rotating microphone array at the United Technologies Research Center. The mean flow field needed for the calculations was obtained from RANS. The results, shown in Figure 21, indicate that the predictions are similarly good as for the subsonic jets. The results are mixed; in some instances, the predictions are excellent (e.g., St=0.3, m=1), while others are not as close (e.g., St=0.3, m=0), with the trend being towards overshoot followed by rapid decay.
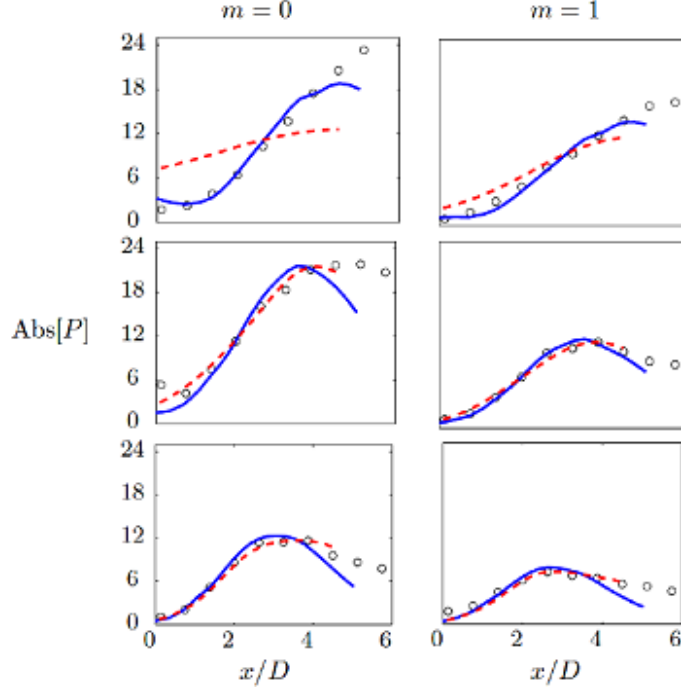
Figure 20 Comparison of microphone near-field array measurements from Suzuki & Colonius (2006) (symbols) with predictions of linear stability analysis from Suzuki & Colonius (2006) (red line) and present linear PSE (blue line) of a cold *M*=0.9 jet.

V. The Wave-Packet Component of the Integrated Tool

To calculate the jet acoustic field, our approach uses a transfer function relating the acoustic far-field to pressure space-time correlations in the jet hydrodynamic near-field. The "hydrodynamic" field refers to the region just outside the turbulent shear layer where the pressure field is dominated by the signatures of large scale turbulence, known to be the source of peak radiation in the aft quadrant. This approach has been validated by the authors by applying the transfer function to direct measurements of two-point pressure statistics in the hydrodynamic field, and demonstrating that the result matches direct measurements of the acoustic field. Additional details can be found in Reba et al. (2005).

The acoustic transfer function is determined by using the Green's function G satisfying the reduced wave equation

$$\nabla^2 G + k^2 G = \delta(x - x')$$ (24)

where k is the acoustic wave number, x is the field point, and x' is the source point. We consider a tailored Green's function satisfying $G=0$ on a conical near-field surface. An analytical solution for G is obtained using a spherical-polar coordinate system (r,ϕ,θ) centered on the virtual origin of the near-field surface. Fourier-spectral representation is used in the azimuthal coordinate ϕ. The resulting equation is solved by first applying a spherical Hankel transform in the radial coordinate r, followed by an expansion in associated Legendre functions in the polar angle θ. The acoustic pressure field p_m at azimuthal mode m can then be expressed in the form

$$p_m(r',\theta') = \int P_m(r,\theta_0) \frac{\partial G_m}{\partial \theta}(r,\theta_0;r',\theta')dr$$ (25)

where P is the pressure on the near-field surface $\theta= \theta_0$ determined from PSE. The governing equations for the PSE component of the integrated analysis tool is contained in Appendix A of this abstract; the equations for the wave-packet method are contained in Appendix B.

21
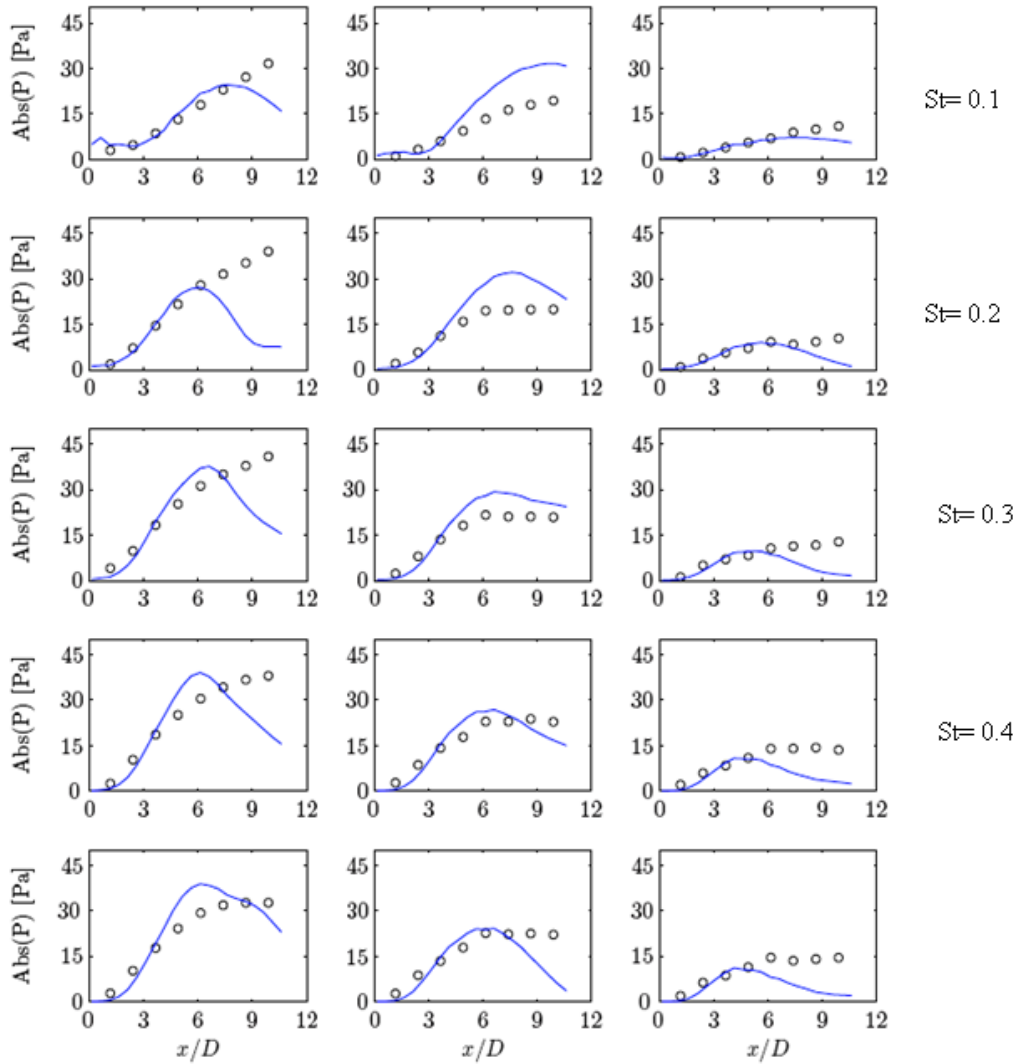
Figure 21 Phased-array microphone measurements (symbols) compared with predictions of linear PSE (blue line) analysis of a cold, supersonic *M*=1.5 jet (B118). These calculations are on-going and will be reported in the final paper.

A. Validating the Wave-packet project method

An analytical method for projecting near-field pressure waveforms to the acoustic far-field was codified by UTRC and delivered to CIT and TTC for implementation into the integrated tool.

The acoustic projection methodology was developed and validated under a concurrent NAVAIR-funded effort. To validate the methodology, a novel rotating array was developed to measure the pressure signatures of large-scale structures in the near-field of a model scale M_j=1.5 jet operating over a range of temperature ratios. The rotating near-field array concept uses two linear arrays situated within 2 diameters of the jet centerline, and approximately following the downstream spread of the shear layer. One linear array can be rotated automatically in the azimuthal direction. The second array is fixed, and provides a reference signal for determining the azimuthal modal content of the near-field pressure. The near-field unsteady pressure data was projected to the acoustic field by solving the linear wave equation with pressure specified on the conical surface defined by the array. The resulting projected field was then compared to direct measurements of the jet acoustic far-field.

Comparisons of the measured and projected far-field are shown in Figure 22 for the test conditions listed in Table 1. The model scale jet was designed by the method of characteristics to provide ideal expansion or shock free flow at the nozzle exit. Overall agreement between measurement and projection is very good at the Strouhal spectral peak, St=0.4, which dominates supersonic jet noise in the aft direction. Discrepancies apparent at the aft-most angles for the unheated condition are most likely the result of insufficient downstream extent of the array; further discussion can be found elsewhere. It can be inferred that a sufficiently accurate prediction of the near-field pressure will provide comparable agreement with the far-field data.

(a) B118;St=0.4   (b) B120;St=0.4   (c) B122;St=0.4
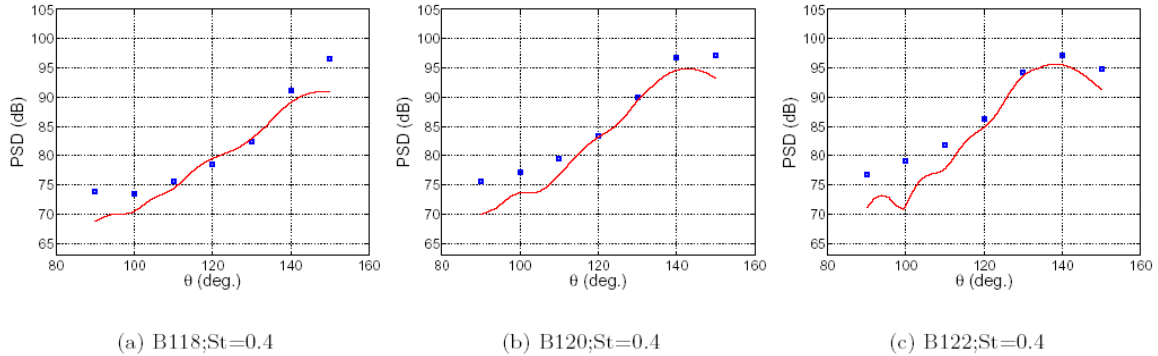
Figure 22 Comparison of measured (symbols) and projected (solid) sound pressure along far field array for B118, B120, and B122 at St=0.4.

VI.   Converting the PSE Code into the AEROFLO Format

The PSE procedure, with the supporting codes, was developed by the Caltech team member, but the integrated prediction tool is being developed in AEROFLO at TTC. Since the computer languages used in the two environments are different, the need exists to convert the procedure at Caltech, which is based on Matlab, to those in AEROFLO, which are based on Fortran, C, C++, and VB. Figures 23 through 26 show the comparison of the selected results obtained with the original PSE code developed at Caltech with the
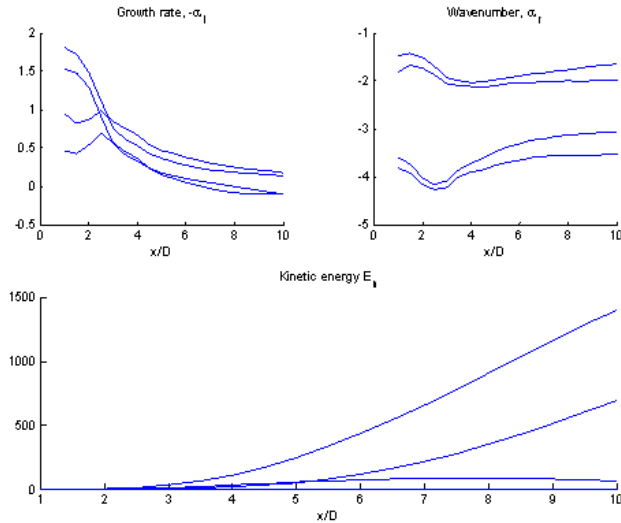
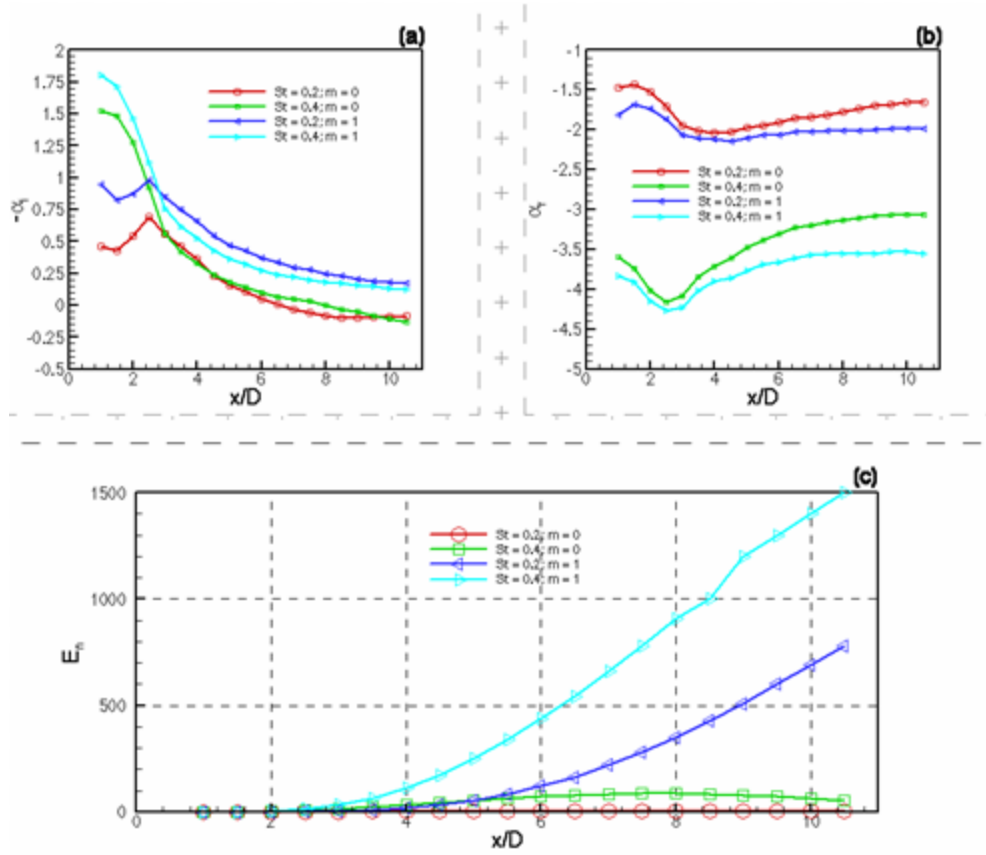**Figure 23 Growth rate, wavenumber, and kinetic energy computed with Matlab in the original PSE code**

23

**Figure 24 Growth rate, wavenumber, and kinetic energy
computed with AEROFLO in the converted PSE code**
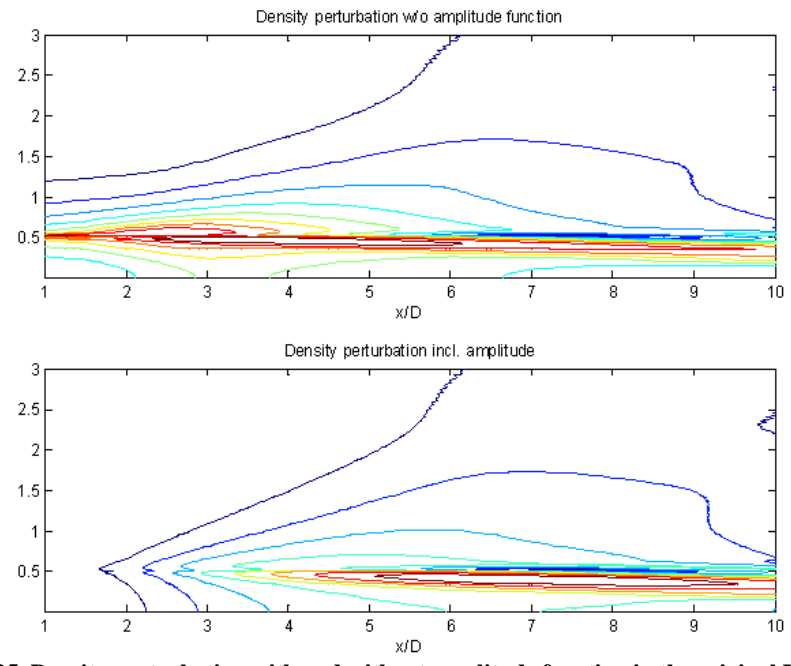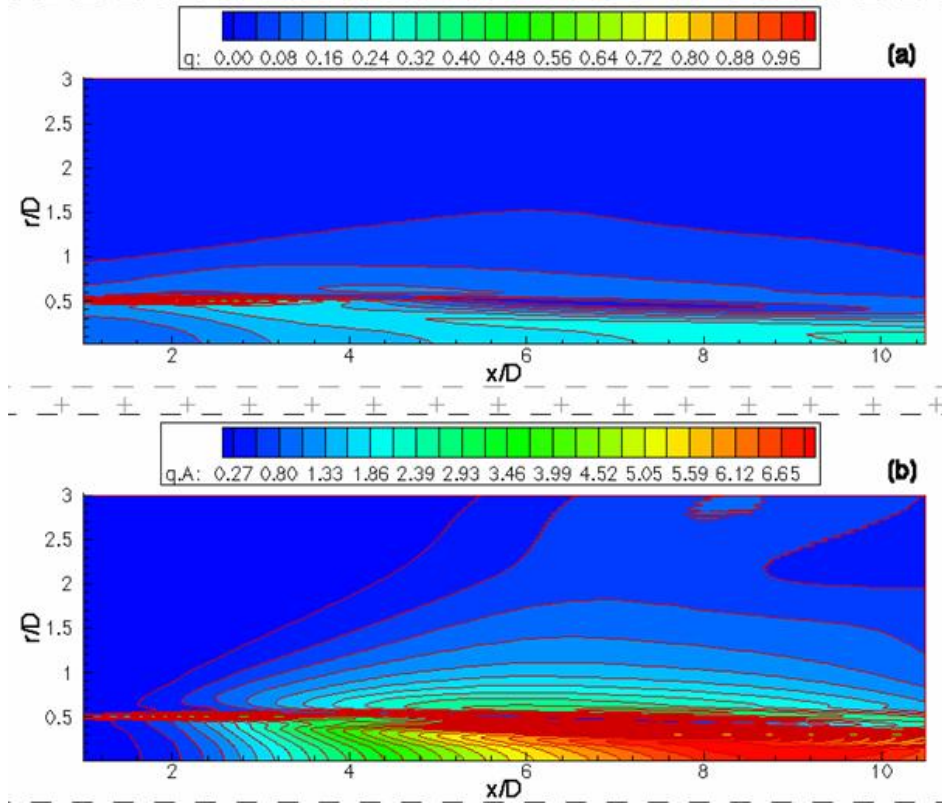

Figure 25 Density perturbation with and without amplitude function in the original PSE code

24

**Figure 26 Density perturbation with and without amplitude function
in computed with AEROFLO in the converted PSE code**

AEROFLO version of the same PSE code. Agreement is evident, indicating that the PSE approach has been successfully integrated into AEROFLO.

VII. Converting the Wave-packet Code into the AEROFLO Format

The wave-packet procedure, with the supporting codes, was developed by the UTRC team member, but the integrated prediction tool is being developed in AEROFLO at TTC. Since the computer languages used in the two environments are different, the need exists to convert the procedure at UTRC, which is based on Matlab, to those in AEROFLO, which are based on Fortran, C, C++, and VB. The original and converted programs were used to project an analytic source function:

$$p(r,\theta) = \frac{e^{irD}}{rD} , \qquad (26)$$

whose expected far field result is

$$p(r',\theta') = \frac{e^{ir'D}}{r'D} . \qquad (27)$$

A comparison of the original and converted codes, the surfaces, original acoustic signal, analytic projected value, and wave-packet calculations compared to the expected results are presented in Figures 27 through 29.
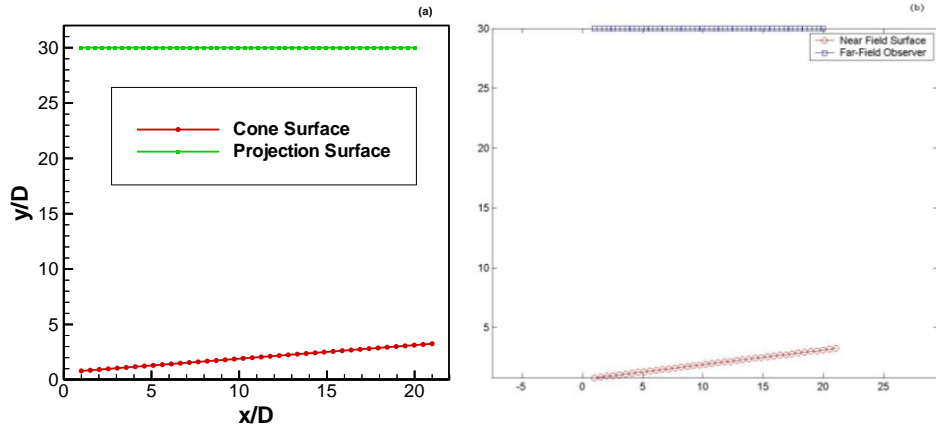
Figure 27 Comparison of the surfaces of the projection code
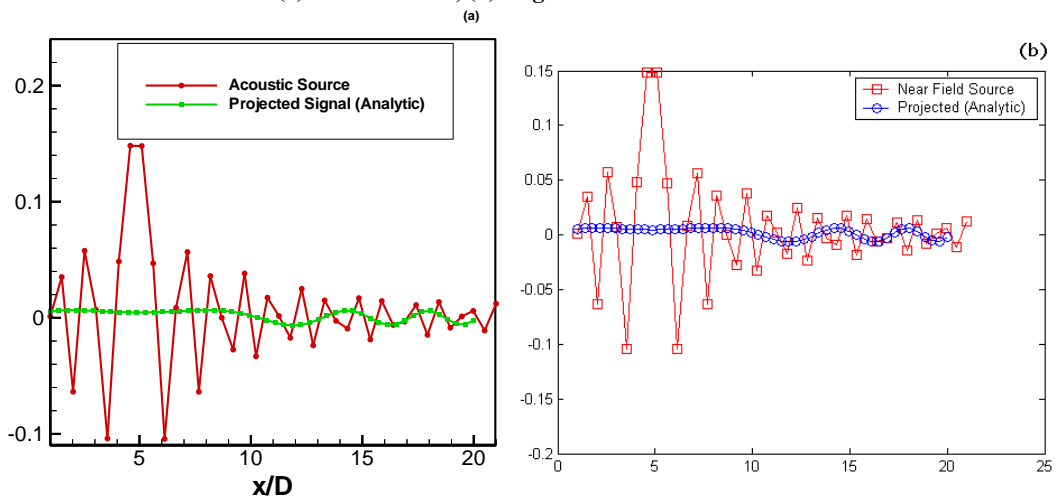**(a) in AEROFLO, (b) original Matlab code at UTRC.**

Figure 28 Comparison of the source signal projected
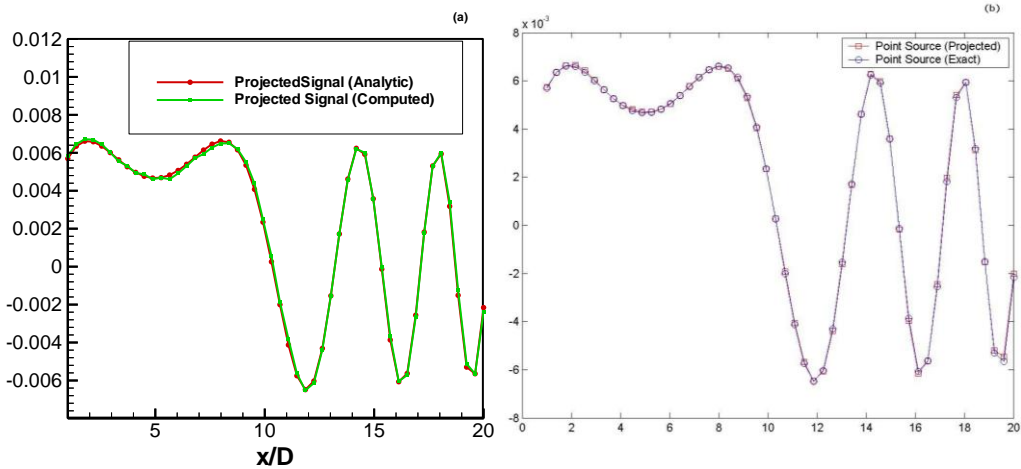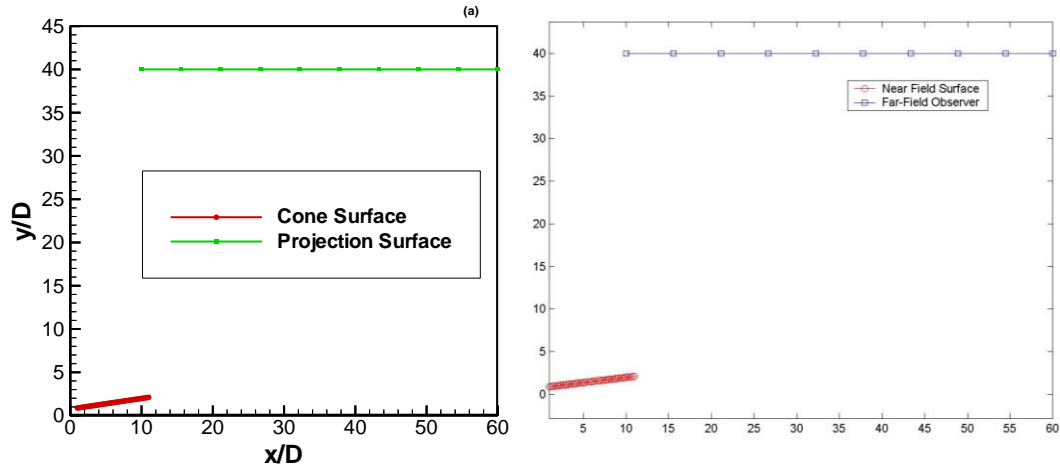**(a) in AEROFLO, (b) original Matlab code at UTRC**

Figure 29 Comparison of the pressure signals projected
(a) in AEROFLO, (b) original Matlab code at UTRC

The agreement between the procedure in the integrated tool (AEROFLO) and in the original procedure at UTRC is evident. We also considered a second problem, with the analytical, near-field source of

26

$$p(r,\theta) = e^{i\frac{2\pi Stx}{0.7}} e^{\left(\left[\frac{x-xs}{L}\right]^2\right)} \quad , \tag{28}$$

where $St = 0.4$, $xs = 5$, and $L = 2.0$.

The comparison is shown in Figures 30 through 32. Again, agreement is evident, indicating that the wave-packet procedure has been successfully implemented in the integrated tool.

Figure 30 Comparison of the surfaces of the projection code
(a) in AEROFLO, (b) original Matlab code at UTRC.
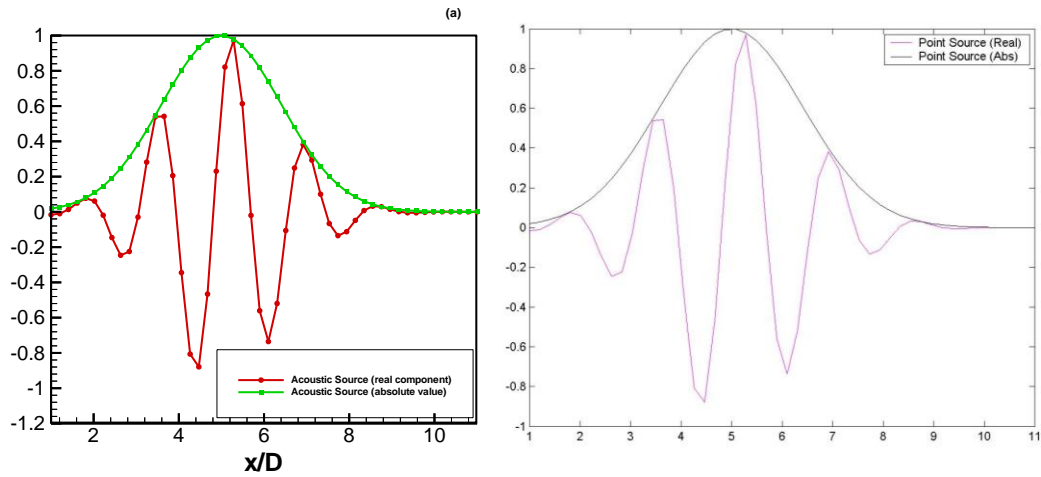
Figure 31 Comparison of the source signal projected
(a) in AEROFLO, (b) original Matlab code at UTRC.

27

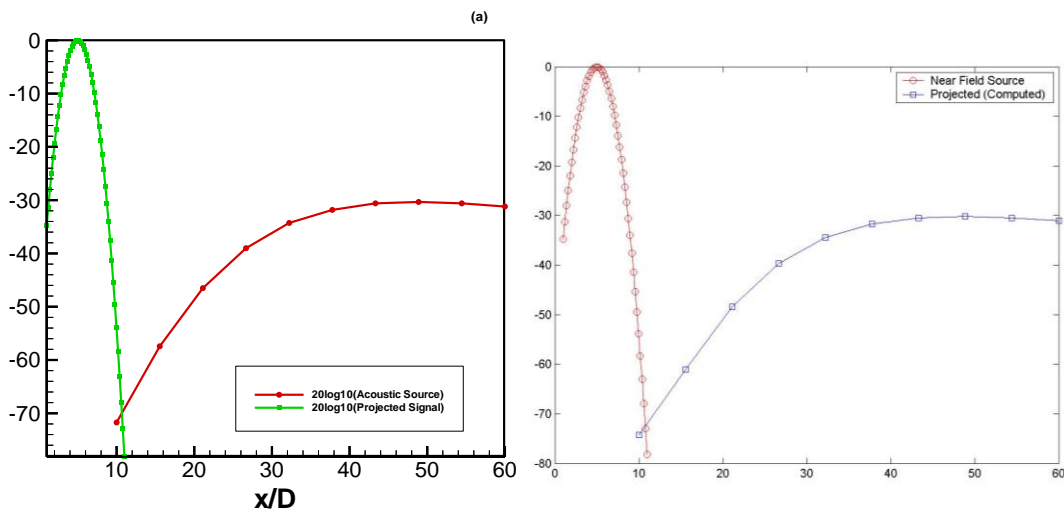**Figure 32 Comparison of the pressure signals projected
(a) in AEROFLO, (b) original Matlab code at UTRC**

VIII.   Concluding remarks

This paper presents the progress in an on-going research program between three organizations to develop and demonstrate innovative, highly-efficient computational methodologies for simultaneous nozzle acoustic and aerodynamic design applicable to subsonic and supersonic jet exhaust noise reduction in tactical aircraft. The approach comprises of three major elements: (1) Reynolds-averaged Navier-Stokes (RANS)-CFD for computing the jet turbulent mean flow, (2) pressure wave packet-based methods for predicting near-field sound generation from the largest scales, based on the Linear Parabolized Stability Equations (LPSE) and the aforementioned RANS solutions, and (3) a method based on the solution of the linear wave equation for determining the acoustic radiation field from the LPSE solution. The individual component of the methodology is presented in terms of its accuracy and robustness. The integration and relationship between the components is discussed and the solutions of the respective sets of model equations have been translated into a common metric for a seamless integration. An end-to-end application of the methodology has almost been completed and will soon be presented after a rigorous validation exercise currently underway.

Acknowledgements

References

Bertolotti, F. P. and Herbert, T., "Analysis of the Linear Stability of Compressible Boundary Layers Using the PSE," Theoretical and Computational Fluid Dynamics, Vol. 3, pp. 117-124, 1991.Bodony, D.J. and Lele, S.K. "A review of the current status of jet noise predictions using large-eddy simulation," 44th AIAA Aerospace Sciences Meeting and Exhibit, AIAA paper 2006-486.

Bridges, J. and Brown, C., "Parametric Testing of Chevrons on Single Flow Hot Jets," 10th AIAA/CEAS Aeroacoustics Conference, Manchester, UK, May 2004, AIAA 2004-2824.

Day, M., Reynolds, W., and Mansour, N., Nonlinear Stability and Structure of Compressible Reacting Mixing Layers, J. Fluid Mech. 451:375-408, 2001.

Gudmundsson, K. and Colonius, T. Spatial stability analysis of chevron jet profiles. AIAA Paper 2007-3599. 13th AIAA/CEAS Aeroacoustics Conference, Rome, May 2007.

Herbert, T., "Parabolized Stability Equations," Annul. Rev. Fluid Mech., Vol. 29, pp. 245–283, 1997.

Jiang, G. and Shu, C.-W. 1996. "Efficient implementation of weighted ENO schemes," *J. Comp. Phys*. 126, pp. 202-228.

Ladeinde, F. , Cai, X.C., Alabi, K., & Safta, C. "The First High-Order CFD Simulation of Aircraft: Challenges and Opportunities," AIAA 2006-1526, Reno, NV, January 2006

Liu, J. T. C., "Developing Large-scale Wavelike Eddies and the Near Jet Noise Field," J. Fluid Mech., Vol. 62, pp. 437–464, 1974.

Malik, M. R. and Chang, C. L., "PSE applied to Supersonic Jet Instability," 35th AIAA Aerospace Sciences Meeting, Reno, NV, January 1997, AIAA 1997-0758.

Michalke, A. and Fuchs, H. V., "On Turbulence and Noise of an Axisymmetric Shear Flow," J. Fluid Mech., Vol. 70, pp. 179–205, 1975.

Pulliam, H. T. and Chaussee, D. S. 1981. A diagonal form of an implicit approximate-factorization algorithm *J. Comp. Phys*. 39 (2), pp. 347.

Reba, R.A., Narayanan, S., Colonius, T. and Suzuki, T., "Modeling Jet Noise from Organized Structures Using Near Field Hydrodynamic Pressure", 11th AIAA/CEAS Aeroacoustics Conference, Monterey, CA, May 2005, AIAA 2005-3093.

Ryu, J., Lele, S.K. and Viswanathan, K., "Investigation of the Role of Instability Waves in Jet Noise Radiation," 46th AIAA Aerospace Sciences Meeting, Reno, NV, January 2008, AIAA 2008-26.

Shu, C.-W., 1997, "Essentially Non-Oscillatory and Weighted Essentially Non-Oscillatory Schemes for Hyperbolic Conservation Laws," NASA CR-97-206253, ICASE Rep. No. 97-65.

Suzuki, T. and Colonius, T., "Instability Waves in a Subsonic Round Jet Detected using a Near-Field Phased Microphone Array," J. Fluid Mech., Vol. 565, pp. 197-226, 2006.

Tam, C.K.W. and Burton, D.E., "Sound Generated by Instability Waves of Supersonic Flows," Part 2, Axisymmetric Jets," J. Fluid Mech., Vol. 138, pp. 273-295, 1984.

Tanna, H.K., Dean P. D. and Burrin, R. H., "The Generation and Radiation of Supersonic Jet Noise, Part III, Turbulent Mixing Noise Data," AFAPL–TR–76–65, 1976.

Tanna H.K., "An experimental study of jet noise, part I: Turbulent Mixing Noise." J. of sound and vibration (1977), 50(3):405-428.

APPENDIX A

Details of the PSE Component of the Integrated Tool

For simplicity, initially considering a 2D jet, we decompose variables as $u' = \overline{U}(x,y) + u$, $v' = \overline{V}(x,y) + v$, $\rho' = 1 + \rho$ and $p' = 1/\gamma + p$, where for simplicity we assume the base flow has no temperature gradients (cold flow). After substitution into the Euler equations, we find

$$\frac{\partial \rho}{\partial t} + \overline{U}_j \frac{\partial \rho}{\partial x_j} + \frac{\partial u_j}{\partial x_j} = -u_j \frac{\partial \rho}{\partial x_j} - \rho \frac{\partial u_j}{\partial x_j} \qquad (A.1)$$

$$\frac{\partial u_i}{\partial t} + \overline{U}_j \frac{\partial u_i}{\partial x_j} + u_j \frac{\partial \overline{U}_i}{\partial x_j} + \frac{\partial p}{\partial x_i} = -\left(u_j + \rho u_j + \rho \overline{U}_j\right)\frac{\partial u_i}{\partial x_j} - \rho \frac{\partial u_i}{\partial t} - \rho u_j \frac{\partial \overline{U}_i}{\partial x_j} \qquad (A.2)$$

$$\frac{\partial p}{\partial t} + \overline{U}_j \frac{\partial p}{\partial x_j} + \frac{\partial u_j}{\partial x_j} = -u_j \frac{\partial p}{\partial x_j} - \gamma p \frac{\partial u_j}{\partial x_j} , \qquad (A.3)$$

where $i=1,2$. Let $q = [u, v, \rho, p]^T$, and decompose this according to PSE:

$$q(x, y, t) = \sum_n \hat{q}_n(x, y) \mathcal{A}_n(x) e^{-i\omega_n t} , \qquad (A.4)$$

where $\hat{q}$ represents the 'slowly-varying' part of the solution, while

$$\mathcal{A}_n(x) = \varepsilon_n e^{i \int^x \alpha_n(\xi) d\xi} \qquad (A.5)$$

captures streamwise growth and wave behavior. Substituting this into the system above, we obtain

$$L_n \hat{q}_n = \frac{\mathcal{F}_n(q_n)}{\mathcal{A}_n} , \qquad (A.6)$$

where L and $\mathcal{F}$ are linear, and non-linear operators, respectively. Let us ignore the non-linear terms for now (set $\mathcal{F}_n = 0$). L_n is

$$L_{\mathcal{N}} = \begin{pmatrix} -i\omega_n + \overline{U}\left(\partial_x + i\alpha_n\right) + \overline{V}\partial_y + \overline{U}_x & \overline{U}_y & \partial_x + i\alpha_n \\ \overline{V}_x & -i\omega_n + \overline{U}\left(\partial_x + i\alpha_n\right) + \overline{V}\partial_y + \overline{V}_y & \partial_y \\ \partial_x + i\alpha_n & \partial_y & -i\omega_n + \overline{U}\left(\partial_x + i\alpha_n\right) + \overline{V}\partial_y \end{pmatrix}.$$

$$(A.7)$$

This is most often split up into two separate operators, $L = L + M\partial_x$, where L contains no streamwise derivatives. Given $\hat{q}^i \equiv \hat{q}(x_i, y)$, $\hat{q}^{i+1}$ is obtained via

$$\left(\Delta x L^{i+1} + M^{i+1}\right)\hat{q}^{i+1} = M^{i+1}\hat{q}^i \qquad (A.8)$$

where first-order implicit differences have been used for the streamwise derivative. Note that L^{i+1} depends on α^{i+1}, an unknown. Thus, an extra condition must be imposed update α between x_i and x_{i+1}. This condition determines the split in downstream evolution between $\hat{q}(x, y)$, and $\mathcal{A}(x)$.

In linear stability analysis (LST), the logarithmic, streamwise derivative of q is

$$-i(\log q)_x = \alpha , \qquad (A.9)$$

while the corresponding PSE quantity is

$$-i(\log q)_x = \alpha - i\frac{\hat{q}_x}{\hat{q}}. \tag{A.10}$$

Having similar definitions of γ between LST and PSE is of value. This, of course, cannot be accomplished directly, correspondence being obtained in an integral sense: multiply by $\hat{q}*\hat{q}$ and integrate over the cross-stream coordinate (and divide by integral of same quantity):

$$\frac{\int_\Omega -i|\hat{q}|^2 (\log q)_x dy}{\int_\Omega |\hat{q}|^2 dy} = \alpha - i\frac{\int_\Omega \hat{q}*\hat{q}_x dy}{\int_\Omega |\hat{q}|^2 dy}. \tag{A.11}$$

If we can now choose α such that $\int_\Omega \hat{q}*\hat{q}_x dy = 0$, then, side by side, the two definitions are

$$\alpha = -i(\log q)_x \quad \text{and} \quad \alpha = -i\frac{\int_\Omega |\hat{q}|^2 (\log q)_x dy}{\int_\Omega |\hat{q}|^2 dy}. \tag{A.12}$$

For jets in cylindrical coordinates, we set $u = u_x$, $v = u_r$, and $w = u_\theta$. We decompose variables as $u = \overline{U}(x,r)+u'$, $v = \overline{V}(x,r)+v'$, $w = w'$, $\rho = \overline{\rho}(x,r)+\rho'$, and $p = 1/\gamma + p'$. Substituting this decomposition into the inviscid Euler equations in cylindrical coordinates results in

$$\overline{\rho}\left(u_t + \overline{U}u_x + \overline{V}u_r + \overline{U}_x u + \overline{U}_r v\right) + p_x = f^1$$
$$\overline{\rho}\left(v_t + \overline{U}v_x + \overline{V}v_r + \overline{V}_x u + \overline{V}_r v\right) + p_r = f^2$$
$$\overline{\rho}\left(w_t + \overline{U}w_x + \overline{V}w_r + \frac{\overline{V}}{r}w\right) + \frac{1}{r}p_\theta = f^3$$
$$\rho_t + \overline{U}\rho_x + \overline{V}\rho_r + (\overline{\rho}u)_x + \frac{1}{r}(r\overline{\rho}v)_r + \frac{1}{r}\overline{\rho}w_\theta = f^4 \tag{A.13}$$
$$p_t + \overline{U}p_x + \overline{V}p_r + u_x + \frac{1}{r}(rv)_r + \frac{1}{r}w_\theta = f^5$$

where

$$f = \begin{pmatrix} -(\overline{\rho}+\rho)\left(uu_x + vu_r + \frac{1}{r}wu_\theta\right) - \rho\left(u_t + \overline{U}u_x + \overline{V}u_r + \overline{U}_x u + \overline{U}_r v\right) \\ -(\overline{\rho}+\rho)\left(uv_x + vv_r + \frac{1}{r}wv_\theta - \frac{w^2}{r}\right) - \rho\left(v_t + \overline{U}v_x + \overline{V}v_r + \overline{V}_x u + \overline{V}_r v\right) \\ -(\overline{\rho}+\rho)\left(uw_x + vw_r + \frac{1}{r}ww_\theta + \frac{1}{r}vw\right) - \rho\left(w_t + \overline{U}w_x + \overline{V}w_r + \frac{\overline{V}}{r}w\right) \\ -(\rho u)_x - (\rho v)_r - \frac{1}{r}(\rho w)_\theta \\ -up_x - vp_r - \frac{1}{r}wp_\theta - \gamma p\left(u_x + \frac{1}{r}(rv)_r + \frac{1}{r}w_\theta\right) \end{pmatrix}$$

31

Represent this more compactly as

$$\mathcal{L}q = \mathbf{f}(q),\qquad\qquad(A.14)$$

where $q = [u,v,w,\rho,p]^T$. $\mathcal{L}$ is a linear operator, which reduces to the LST operator upon setting $\overline{V} = \overline{U}_x = \overline{\rho}_x = 0$.

In the cylindrical case, the PSE assumption is

$$q(x,r,\theta,t) = \sum_{m,n}\hat{q}_{mn}(x,r)A_{mn}(x)e^{i(m\theta-\omega_n t)},\qquad\qquad(A.15)$$

-where

$$A_{mn}(x) = \varepsilon_{mn}e^{i\int^x \alpha_{mn}(\xi)d\xi},\qquad\qquad(A.16)$$

where ε_{mn} is the initial level of mode mn. Substituting this into the above equations results in

$$\left[\overline{\rho}\left(-i\omega_n + \overline{U}(\partial_x + i\alpha) + \overline{V}\partial_r + \overline{U}_x\right), \overline{\rho}\,\overline{U}_r, 0, 0, \partial_x + i\alpha\right]\cdot\hat{q}_{mn} = \mathbf{f}^1_{mn}/A_{mn}$$

$$\left[\overline{\rho}\,\overline{V}_x, \overline{\rho}\left(-i\omega_n + \overline{U}(\partial_x + i\alpha) + \overline{V}\partial_r + \overline{V}_r\right), 0, 0, \partial_r\right]\cdot\hat{q}_{mn} = \mathbf{f}^2_{mn}/A_{mn}$$

$$\left[0, 0, \overline{\rho}\left(-i\omega_n + \overline{U}(\partial_x + i\alpha) + \overline{V}\partial_r + \frac{\overline{V}}{r}\right), 0, \frac{im}{r}\right]\cdot\hat{q}_{mn} = \mathbf{f}^3_{mn}/A_{mn}$$

$$\left[\overline{\rho}_x + \rho(\partial_x + i\alpha), \frac{\overline{\rho}}{r} + \overline{\rho}_r + \overline{\rho}\partial_r, \overline{\rho}\frac{im}{r}, -i\omega_n + \overline{U}(\partial_x + i\alpha) + \overline{V}\partial_r, 0\right]\cdot\hat{q}_{mn} = \mathbf{f}^4_{mn}/A_{mn}$$

$$\left[\partial_x + i\alpha, \frac{1}{r} + \partial_r, \frac{im}{r}, 0, -i\omega_n + \overline{U}(\partial_x + i\alpha) + \overline{V}\partial_r\right]\cdot\hat{q}_{mn} = \mathbf{f}^5_{mn}/A_{mn}$$

or

$$L_{mn}\hat{q}_{mn} = \frac{\mathbf{f}_{mn}}{A_{mn}}\qquad\qquad(A.17)$$

APPENDIX B

Details of the Wave Packet Component of the Integrated Tool

B.0 The Wave Packet Projection Method

The governing equation can be written as:

$$\nabla^2 p + k^2 p = 0$$
$$\frac{\partial^2 T}{\partial t^2} - \omega^2 T = 0,\qquad\qquad(B.1)$$

where $\omega = kc$ is the acoustic wavelength.

The first equation is the Helmholtz equation, which lends itself to analytic solutions in form of Green's functions

$$\nabla^2 G + k^2 G = \delta(\vec{r} - \vec{r}'), \tag{B.2}$$

where

$$p(\vec{r}') = \int G(\vec{r}', \vec{r}) p(\vec{r}) d\vec{r}. \tag{B.3}$$

Following the formulation in Reba et al. (2008), near-field acoustic data assumed known on a conical surface is projected in space by solving the above linear wave equation. The boundary condition $G = 0$ is imposed on the conical surface, and the equation is solved in a spherical coordinate system centered on the virtual origin of the cone surface. The polar angle θ is oriented such that $\theta = \pi$ corresponds to the jet axis and the cone surface is defined as $\theta = \theta_0$. Utilizing a Fourier transform in the azimuthal direction,

$$G_m = \frac{1}{2\pi} \int G(\phi) e^{im\phi} d\phi \tag{B.4}$$

Eq. 5 in spherical coordinates becomes:

$$\left[\frac{1}{r^2} \frac{\partial}{\partial r} \left(r^2 \frac{\partial}{\partial r} \right) + \frac{1}{r^2 \sin\theta} \frac{\partial}{\partial \theta} \left(\sin\theta \frac{\partial}{\partial \theta} \right) + \frac{1}{r^2 \sin^2\theta} \frac{\partial^2}{\partial \phi^2} + k^2 \right] G_m = \delta(\vec{r} - \vec{r}'). \tag{B.5}$$

On expanding the left hand operator, this becomes:

$$\frac{1}{r^2 \sin\theta} \left[\sin\theta \frac{\partial}{\partial r} \left(r^2 \frac{\partial G_m}{\partial r} \right) + \frac{\partial}{\partial \theta} \left(\sin\theta \frac{\partial G_m}{\partial \theta} \right) - \frac{m^2 G_m}{\sin\theta} \right] + k^2 G_m = \frac{\delta(r - r')\delta(\theta - \theta')}{2\pi r^2 \sin\theta} e^{im\phi'}. \tag{B.6}$$

Introducing the spherical Hankel transform in the radial direction,

$$G_m(\nu, \theta) = \int_0^\infty G_m(r, \theta) H_{\nu+1/2}(kr) \frac{dr}{\sqrt{r}}, \tag{B.7}$$

$$\left[\frac{1}{\sin\theta} \frac{\partial}{\partial \theta} \left(\sin\theta \frac{\partial G_m(\nu, \theta)}{\partial \theta} \right) + \left(\nu(\nu+1) - \frac{m^2}{\sin^2\theta} \right) G_m(\nu, \theta) \right] = \frac{\delta(\theta - \theta')}{\sin\theta} \frac{H_{\nu+1/2}(kr')}{\sqrt{r}'} e^{im\phi'}. \tag{B.8}$$

Representing the Green's function based on the Legendre functions $P_\mu^m(\cos\theta)$ associated with the eigenvalues μ determined by enforcing the boundary condition $P_\mu^m(\cos\theta) = 0$,

$$G_m(\nu, \theta) = \sum_\mu a_\mu P_\mu^m(\cos\theta). \tag{B.9}$$

The coefficients of the basis expansion in Eqn. 12 can be determined by applying the transform

$$\int_0^{\theta_0} f(\theta) \sin\theta P_\mu^m(\cos\theta) d\theta \tag{B.10}$$

to Eqn. 11 to obtain

$$G_m(\nu, \theta) = \frac{e^{im\phi'}}{\sqrt{r'}} \sum_\mu \frac{1}{A_\mu} \frac{H_{\nu+1/2}(kr') P_\mu^m(\cos\theta) P_\mu^m(\cos\theta')}{\nu(\nu+1) - \mu(\mu+1)}, \tag{B.11}$$

where

$$A_\mu = \int_0^{\theta_0} \sin\theta \left| P_\mu^m(\cos\theta) \right|^2 d\theta. \tag{B.12}$$

Applying the inverse Hankel transform

$$G_m(r, \theta) = \frac{1}{2\sqrt{r}} \int_{-i\infty}^{i\infty} (\nu + 1/2) G_m(\nu, \theta) J_{\nu+1/2}(kr) d\nu, \tag{B.13}$$

$$G_m(r,\theta) = \frac{1}{2\sqrt{r}} \int_{-i\infty}^{i\infty} (\nu+1/2) \frac{e^{im\phi'}}{\sqrt{r'}} \sum_\mu \frac{1}{A_\mu} \frac{H_{\nu+1/2}(kr')P_\mu^m(\cos\theta)P_\mu^m(\cos\theta')}{\nu(\nu+1)-\mu(\mu+1)} J_{\nu+1/2}(kr)d\nu .$$

(B.14)

Using Eqn. (6), the acoustic field due to a pressure distribution on the near field can be written as

$$p_m(r',\theta') = 2\pi \sin\alpha \int_0^\infty p_m(r,\theta) \frac{\partial G_m(r',\theta',r,\theta)}{\partial \theta} dr ,$$

(B.15)

where α is the array spreading angle or cone half angle.